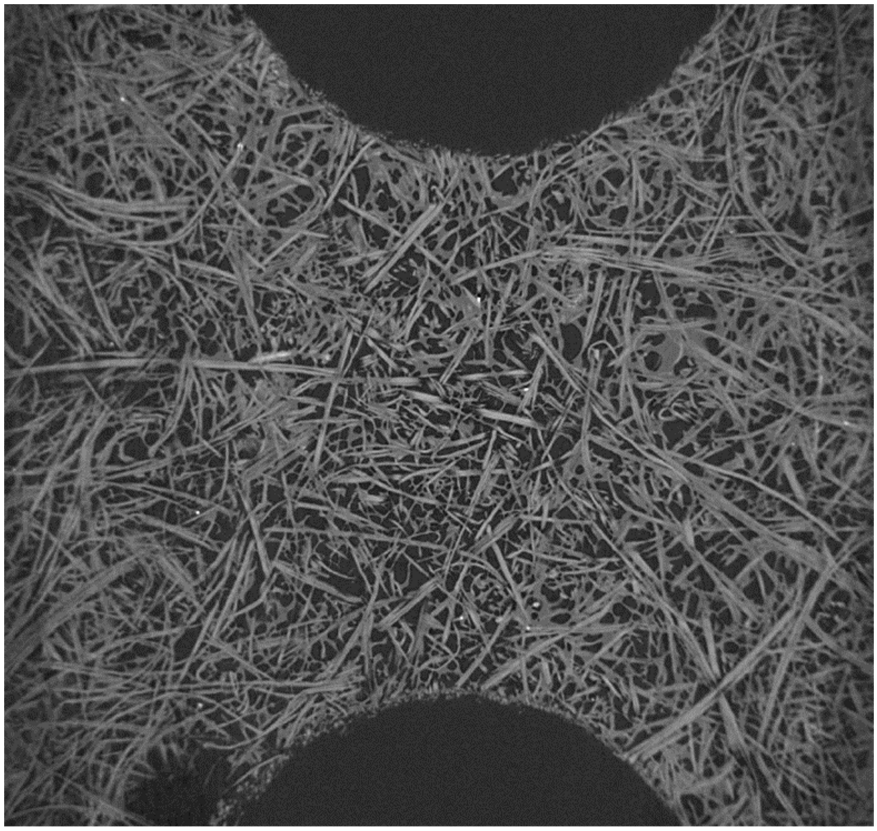

Characterisation of natural fibre composites using X-ray computer tomography aided engineering

Master's thesis in Master Program Structural Engineering and Building Technology

MARCUS IVERSEN
ANTON ÅRMANN

Department of Industrial and Materials Science
Chalmers University of Technology
Master's thesis IMSX30
Gothenburg, Sweden 2023

MASTER'S THESIS IMSX30

Characterisation of natural fibre composites using X-ray computer tomography aided engineering

MARCUS IVERSEN
ANTON ÅRMANN

CHALMERS
UNIVERSITY OF TECHNOLOGY

Department of Industrial and Materials Science
Division of Material and Computational Mechanics
CHALMERS UNIVERSITY OF TECHNOLOGY
Gothenburg, Sweden 2023

Characterisation of natural fibre composites using X-ray computer tomography aided engineering

MARCUS IVERSEN
ANTON ÅRMANN

Supervisors: Adj. Prof. Renaud Gutkin, Volvo Cars Corporation. Department of Industrial and Materials Science, Chalmers University of Technology.
Nikoleta Pasvanti, Volvo Cars Corporation.
Examiner: Prof. Leif Asp, Department of Industrial and Materials Science.

Department of Industrial and Materials Science
Division of Material and Computational Mechanics
Chalmers University of Technology
SE-412 96 Gothenburg
Telephone +46 31 772 1000

Cover: Figure from the image acquisition of one of the samples considered in this thesis.

Typeset in LaTeX
Department of Industrial and Materials Science
Gothenburg, Sweden 2023

Characterisation of natural fibre composites using X-ray computer tomography aided engineering
Marcus Iversen
Anton Årmann
Department of Industrial and Materials Science
Chalmers University of Technology

Abstract

The incorporation of bio-based materials and biocomposites is a crucial component in the pursuit of climate neutrality. Volvo Cars has set a target to achieve climate neutrality by 2040, leading to a growing interest in the application of bio-based materials and biocomposites. This has stimulated research in the field of mechanical behaviour and modelling, using Computer Aided Engineering (CAE) tools. Today there is a lack of Finite Element (FE) and material models for biocomposites, in particular those made of natural fibres as they display a complex microstructure.

Throughout the project three kenaf fibre reinforced composite samples are analysed and characterised. The complex microstructure is obtained from Computer Tomography (CT) scanning, which is a non-destructive method. X-ray computer tomography Aided Engineering (XAE) is used to characterise the nonlinear behaviour of natural fibre composites by creating a FE-model. The FE-model is used in a virtual tensile test and compared against a physical test to calibrate the material properties of the samples. FE-simulations of natural fibre composites based on detailed information of their microstructure lacks in the litterature. To the best of our knowledge, conducting it at the coupon level has not been attempted in research until this day.

The results shows that the characterisation of the microstructure using CT-scanning is successful. Furthermore, the result shows that the XAE process, going from image data to creating a mesh and running a quasi-static FE analysis, is applicable to a natural fibre composite. Thereafter, virtual tests are correlated against the mechanical tests and the material calibration successfully captures the initial stiffness, the non-linearity and the peak load of the samples. Further, the response for different areal weights are successfully predicted using the calibrated mechanical properties.

Keywords: Natural fibre reinforced composite, Computer tomography, Finite element, Material characterisation, Correlation, Virtual testing, XAE, LS-DYNA, RETOMO, Kenaf

Acknowledgements

A special thanks to Renaud Gutkin for the valuable guidance, support and for introducing the project to us. We would also like to thank Nikoleta Pasvanti for daily support and guidance throughout the project. BETA CAE Systems have been included in the project and we would like to thank Stelios Seitanis among others for all support, discussions and for providing us with a workspace when needed.

Prof. Leif Asp has as the examiner of this project supported us along the entire project and continuously underlined the importance of our knowledge, which we are very grateful for. We would also like to thank Robert Auenhammer for all the input and discussions about CT scanning and XAE, and for bringing us to Copenhagen to observe the CT scanning of our samples.

Finally, we would like to thank Volvo Cars for making this thesis project possible and providing us with a workspace, computers, software and all other resources needed. Thanks to the CAE Durability team for including us in the team, answering questions and creating a friendly work environment.

Authors, Gothenburg, May 2023

Contents

List of Figures

List of Tables

1
Introduction

The use of bio-based materials and biocomposites is an important part of achieving climate neutrality. Bio-based materials sequester carbon dioxide during their growth phase and will therefore not release new CO_2 into the atmosphere. Natural fibres used in biocomposites often show good mechanical properties and can offer significant weight savings [1] in comparison to traditional plastics or glass fibre composites.

The use of biocomposites in structural A-surface and bodywork parts has increased the interest in mechanical behaviour and modelling using CAE tools. However, there is today a lack of FE- and material models for biocomposites, in particular those made of natural fibres as they display a complex microstructure. CT scanning and physical testing are tools for obtaining FE- and material model methods. Once a method for this modelling is in place, it enables virtual testing and calibration of the material model.

When introducing new materials, many material tests must be performed to characterise the material properties. This is an expensive and time consuming procedure when performing the physical tests. Therefore, it is of interest to perform these material tests virtually. CT analyses have been performed on man-made fibre-reinforced polymer composites at the coupon level [2] as well as for random oriented natural fibre-reinforced polymer composites on a Representative Volume Element (RVE) level [3], [4]. There is a lack of analysis of random oriented natural fibre composites at the coupon level in the field of research today.

Natural fibre composites come with a number of challenges as they are not man-made. This means that each individual fibre is unique and influenced by the conditions it has been exposed to during its growth. Furthermore, the mechanical properties of the fibre can change during composite manufacture [5]. This will significantly influence the material modelling of these natural fibre composites as the spread in material parameters are extensive.

Given the complexity of natural fibre composites, the main objective of this thesis work is to answer the following question.

- Is it possible to correlate a virtual coupon test to a mechanical test where the underlying basis comes from X-ray computer tomography aided engineering?

Virtual tests for natural fibre composites at the coupon level have not been done before using computer tomography generated image-based FE models. Computer tomography

will enable the characterisation of the composite microstructure. The characteristics of the microstructure are the ratio of the fibre and matrix volume fraction together with the fibre orientation information. As previously stated, computer tomography studies have previously only been performed on man-made fibre composites on the coupon level or with natural fibres on a RVE level. Thus, to date, this is the first research project to address the material characterisation on the fibre as well as coupon level including nonlinear material behaviour and material failure.

This project will be limited to analysis of three different coupons of the same material, a kenaf fibre composite with a polypropylene matrix. All three coupons will be CT scanned, tested physically in a mechanical test and virtually in the computer.

The thesis is structured with six chapters where Chapter 2 describes the theoretical background for the project. Chapter 3 presents the methodology. In Chapter 4, results from all stages of the project are presented. Further, the results are discussed in Chapter 5, whereas some concluding remarks are presented in Chapter 6.

2
Theory

2.1 Fibre reinforced composites

A fibre reinforced composite material consists of two main constituents, fibre and matrix. The fibres are embedded in the matrix material, which together with the polymer matrix forms the fibre reinforced composite, as illustrated in Figure 2.1. These materials can be formed in a number of different ways to ensure that the desired shape of the composite is obtained. One major advantage of using fibre-reinforced composite materials compared to e.g. steel is that it has a much lower weight-to-stiffness ratio [6]. This means that one can obtain the same stiffness in a certain direction with a lighter structure of a fibre reinforced composite compared to the steel structure.

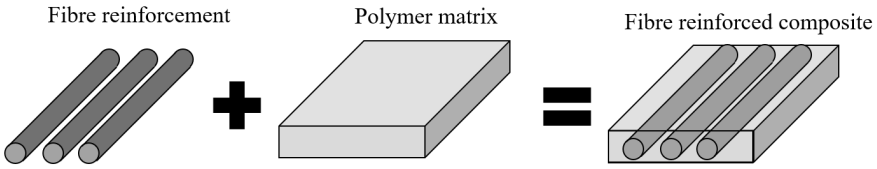

Figure 2.1: The general assembly of a fibre-reinforced composite, inspiration from [6].

The fibre is the primary load-bearing component responsible for imparting excellent mechanical properties to the composite [7]. A number of fibres are available with different properties effective in reinforcing different matrix materials. The mechanical properties of the fibres are most often observed in the fibre direction, which implies that the information on fibre direction is crucial when analysing fibre reinforced composites.

The main function of the matrix is to bind the fibres together. By this, the matrix transfers the loads to the fibres as well as protects the fibres from external influence. The matrix has a strong influence on several mechanical properties of the composite, such as transverse modulus and strength, shear properties, and properties in compression.

2.2 Natural fibre composites

Natural fibre composites are composite materials made of bio-based fibres together with a matrix. There is a number of different natural fibres available. In this thesis the focus will be only on kenaf fibres together with polypropylene (PP) fibres. The mechanical properties of kenaf fibres are within the range of other natural fibres and suit well as fibre

material in a natural fibre reinforced composite [1]. However, according to several different sources, there is a wide range of mechanical properties. The mechanical properties for kenaf fibre are presented in Table 2.1 together with the properties of PP fibre.

Table 2.1: Mechanical properties of kenaf [8] and polypropylene fibre [5], [9].

Mechanical property	Kenaf fibre	Polypropylene fibre
Density [g/cm^3]	0.6 - 1.5	0.9 - 1.0
Tensile modulus [GPa]	10 - 53	0.8 - 2.0
Tensile strength [MPa]	223 - 930	26 - 49
Elongation [%]	1.6 - 10	40 - 500

Manufacturing of natural fibre reinforced composites can be performed in a number of different ways. The bales of raw material, kenaf and polypropylene fibres, are put together, automatically weighed and then put into the mixer. The homogeneous mixture coming from the carding machine is a very smooth web. This web then needs to be bonded which is a mechanical procedure called needling where the web is exposed to needles with the intention to orient the fibres randomly in all three directions of the volume. At this point, a porous non-woven mat of kenaf fibre polypropylene is obtained. To form a consolidated fibre composite a double belt press is used to press the non-woven mixture of natural and polypropylene fibres to a desired thickness. Depending of how much the mat is pressed it will contains different amount of voids. A thinner plate is less porous and contain less amount of voids.

2.3 X-ray computer tomography aided engineering (XAE)

X-ray computer tomography aided engineering (XAE) is a methodology described by Auenhammer and co-workers [2] which serves as a baseline in this thesis. After some modifications and additions to the method, a new process is presented in Section 3.2 in this thesis. The theoretical parts of the XAE process are summarised in Figure 2.2 and are further described in the following section.

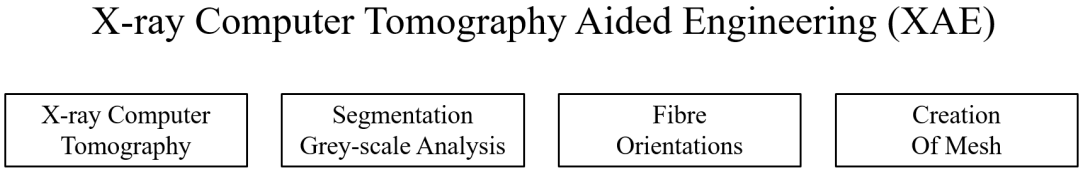

Figure 2.2: X-ray computer tomography aided engineering and its core elements.

X-ray computer tomography was initially introduced in the medical industry in the 1960s and was further developed and later used in non-medical research in the 70s and 80s [2]. In X-ray computer tomography the sample is rotated and exposed to the X-ray beam from different angles in order to generate many 2D projections, the sample could also be fixed when the X-ray source and detector rotate around the sample. Compared to another scanning method, radiography, where all information of the sample is projected in one shot

the X-ray computer tomography gathers more 2D projections enabling further analysis in 3D. This procedure results in a collection of line integrals which need to be reconstructed to obtain a 3D image [10]. After the image acquisition, the following steps are segmentation, fibre tracking and meshing. The segmentation procedure is based on grey-scale thresholds for each of the phases void, matrix and fibre. The fibre tracking is a method where an algorithm projects the propagation of a fibre and can by this reveal information about each fibre direction [11]. The final step, meshing, lumps together multiple pixels from the image data forming solid elements.

An image histogram is a distribution of grey-scale values reflecting the frequency of each grey-scale value [12]. The histogram analysis relies on the premise that the grey-scale values of the object and the background can be distinguished, resulting in two or several peaks being depicted on the histogram, see Figure 2.3. Although these peaks typically overlap, a minimum can be detected between them to facilitate the separation of both objects. The optimal threshold value is at the histogram minimum [13], which corresponds to the point where the derivative is minimal. Due to the minimal variation in the slope of the curve, the sensitivity of the value D_1 in this region is low.

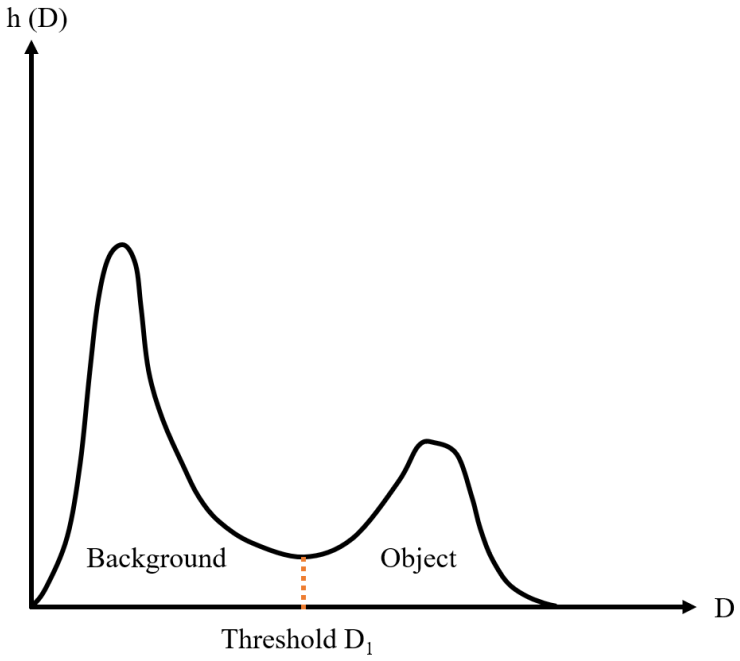

Figure 2.3: An example of how a threshold is determined from a histogram of image data, inspired from [13].

2.4 Mechanical test

The mechanical test of interest in this thesis is a tensile test of a double notched sample. The test will result in a force-displacement response for an uniaxial load case. From the result, one will be able to calibrate a coupon stiffness as well as calibrate the damage parameters of the material. The dimensions of the double notch sample are presented in

Figure 2.4. To capture the strain distribution of the sample, a test procedure with digital image correlation (DIC) can be utilised.

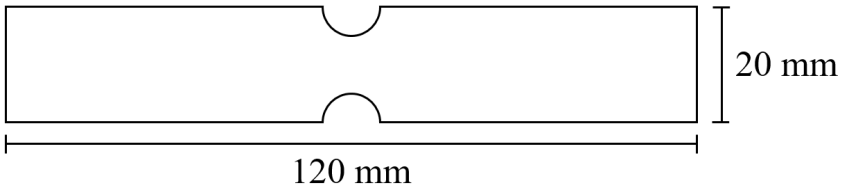

Figure 2.4: The double notch sample with dimensions. The three samples considered have different thicknesses as presented in Table 3.1.

2.4.1 Digital Image Correlation

Digital image correlation (DIC) is a non-contact optical technique to measure surface shape, deformation and strain of a sample [14]. The DIC setup has two key parts being a DIC camera and a tensile test machine. DIC is a technique where digital images of a sample are acquired at different time stages. An algorithm, which tracks the local displacements, is applied to gather information about displacements and strains locally in the different imaged stages. Before the image data can be gathered the sample has to be painted with a black-and-white speckle pattern. Due to this high contrast the algorithm can easily track speckles over time and by that accurately capture the displacement field. This can be made in a number of ways, using paint or powder, the important part is that a pattern with big contrast is applied to the sample [15], [16], [17].

2.5 Material modelling

In this section the considered plasticity and damage models are presented. Both the theory behind the models and the LS-DYNA material cards of choice are presented.

2.5.1 Plasticity model

A plasticity model can be introduced to capture the nonlinear response of the material. In LS-DYNA, one way to do this is to introduce a material model for the matrix material, called *MAT_PIECEWISE_LINEAR_PLASTICITY*, which is a linear plasticity material model [18]. It is possible to include a user-defined flow curve in this material model. The material model includes the von Mises yield criterion that assumes isotropy. Hence, the material is considered elastic as long as the von Mises stress, i.e. the effective stress, is below the yield stress. When the effective stress gets equal to, or higher than, the yield stress the material response is plastic. If a material reaches plasticity there are remaining deformations after unloading. The relation described above can be summarised in a yield function as shown in Equation 2.1 below [19].

$$\phi = \sigma_{vM} - \sigma_y \tag{2.1}$$

Where σ_{vM} is the effective stress and σ_y is the yield stress. The response is elastic if $\phi < 0$ and the response is plastic if $\phi \geq 0$ as described above.

2.5.2 Fibre failure model

A failure can be either brittle or ductile. Figure 2.5 show a typical stress strain response of how the two phenomenon behave during loding.

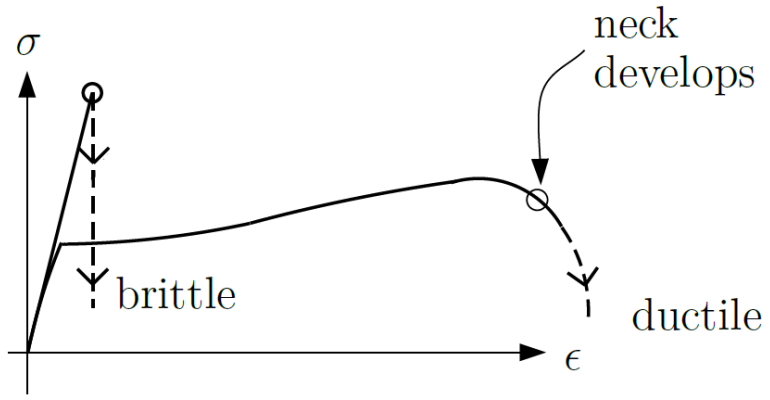

Figure 2.5: Stress strain response of a ductile and brittle damage process, from [19].

One possible failure mode in a fibre composite is the fibre tensile failure which is a brittle failure. This is a failure mode where the longitudinal stresses or strain are so high that the fibres break. One way to model this is by using a strain based failure criterion shown in Equation 2.2.

$$f_{ft} = \frac{\varepsilon_f}{\varepsilon_{fU}} \tag{2.2}$$

The failure criterion states that the fibre tensile failure will occur if $f_{ft} = 1$, i.e. when the longitudinal fibre strain ε_f is higher than the ultimate fibre strain ε_{fU}. To include this in the model, an additional LS-DYNA material card is added to the fibre elements in the model. The material card is called *MAT_ADD_EROSION* [18]. Inside the material card the ultimate principle strain, ε_{fU}, is defined as the strain to failure for the fibre elements. Fibre elements are deleted when the strain in the fibres exceeds the value of ε_{fU}.

2.6 Explicit finite element analysis

The finite element method can be used to solve either static or dynamic structural mechanical problems. When computing non-linearity in materials and geometries a static problem formulation can have convergence issues. This applies in particular when computing damage, which is a highly nonlinear phenomenon [20]. In these cases, it is beneficial using a dynamic formulation, which is presented in Equation 2.3.

$$M\ddot{u} + C\dot{u} + Ku = F \tag{2.3}$$

Where M is the mass matrix, C the damping matrix, K the stiffness matrix and F the external force vector. u, $\dot{u}$ and $\ddot{u}$ represent the displacement, velocity and acceleration vectors.

A dynamic equation can be solved using a direct integration method, an explicit time integration. The explicit time integration uses the characteristics of the mass matrix M and the damping matrix C. If these matrices are diagonolised the equations on the left-hand side in Equation 2.3 is uncoupled and no factorisation is needed [21]. Thus, no iteration procedure is needed and the algorithm is a forward-marching solver.

In order to achieve accurate results from a solution using explicit time integration one must use small time increments. The critical time step is dependent on the material properties and the smallest element size in the model. In Equation 2.4 the conditions of the critical time step [21] are expressed.

$$\Delta t = \alpha \Delta t_{crit} \quad \Delta t_{crit} = \frac{2}{\omega_{max}} \leq \min_{e,I} \frac{2}{\omega_I^e} = \min_e \frac{l_e}{c_e} \tag{2.4}$$

Where ω_{max} is the maximum eigenfrequency, l_e is the length of an element e, c_e is the wave speed in element e, and α is the reduction factor accounting for destabilizing effects. α is equal to 0.9 by default in LS-DYNA [18]. Furthermore, the wave speed in the element is dependent on the element properties according to Equation 2.5.

$$c_e = \sqrt{\frac{E}{\rho(1-\nu^2)}} \tag{2.5}$$

Where E represents the Youngs's modulus, ρ the density and ν the Poisson's ratio.

Physical material tests performed in this work used a quasi-static loading rate. To simulate a virtual test using explicit analysis one cannot use the same loading rate as in the physical test. This is due to the small time steps in the simulation leading to a long computational time. However, the increase of loading rate has to be done with care to not introduce a dynamic effect in the result. In order to confirm that there are no dynamic responses affecting the results, the energy ratio needs to be monitored. The analysis operator should confirm that the kinetic energy remains small in comparison to the total energy in the system. Furthermore, if the computations are time-consuming it can be reduced using mass scaling. Mass scaling reduces the time step size by adding non-physical mass. For the simulation in LS-DYNA mass is added to elements increasing the critical time step and therefore reducing the simulation time [18].

3
Methodology

This chapter covers the methodology of the project where all major stages are described. For a structured project planning, a flow chart of the different stages is made. Figure 3.1 shows the flow chart where all stages of the project are presented.

The structure of the chapter follows the same logic as the flow chart where firstly, the considered samples are presented followed by the XAE process. Then the mechanical tests, with DIC and microscopy, are presented followed by the interpretation of the finite element model. Finally, calibration of the material parameters will take place based on the results from the mechanical tests.

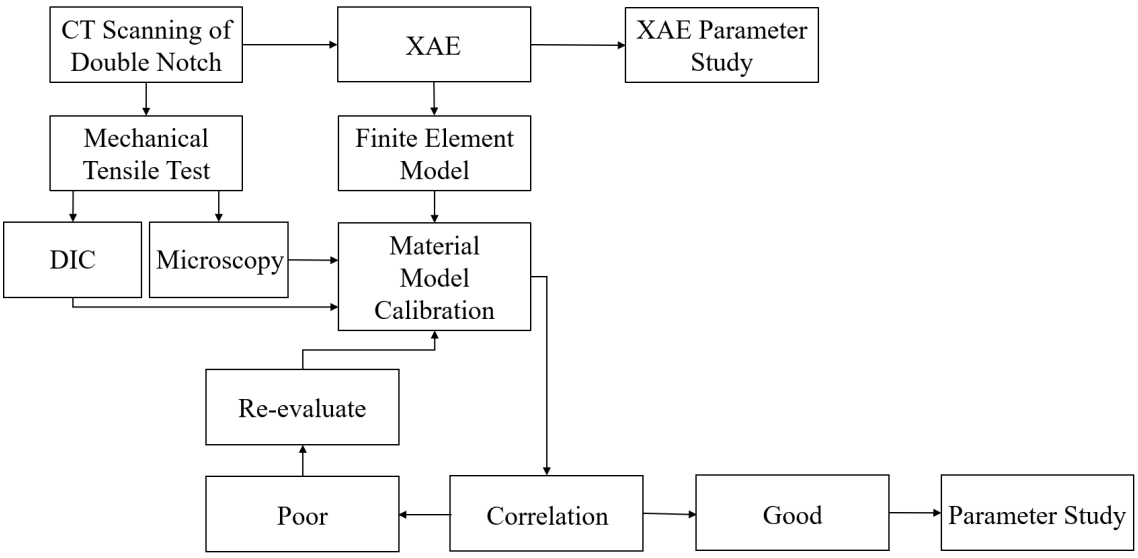

Figure 3.1: Flow chart of the stages in the thesis work.

3.1 Analysed samples

In this study, three different samples are studied. Figure 3.2 shows the three samples prior to testing. All samples are composites with kenaf fibres and polypropylene matrix with a 50/50 weight ratio. There is some variety in both thickness and density among the samples. Material, areal weight, thickness and density are presented for all samples in Table 3.1.

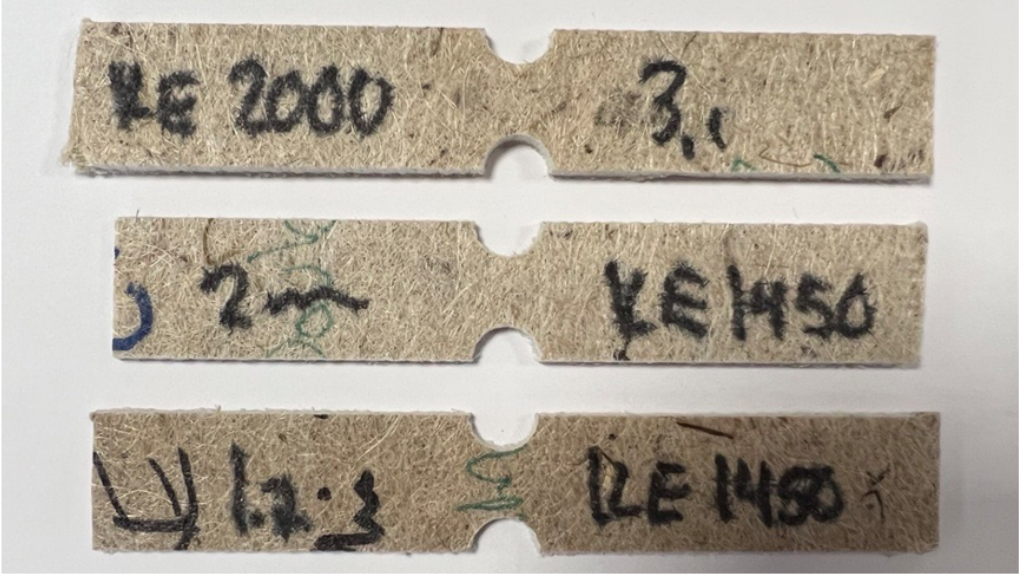

Figure 3.2: Figure showing the three samples prior to testing. Sample 1, 2 and 3 depicted from top to bottom.

Table 3.1: Numbering of samples where material, areal weight, thickness and density are presented.

	Name	Material	Areal Weight	Thickness	Density
Sample 1	KE2000	Kenaf	2000 g/mm^2	3.2 mm	625 g/mm^3
Sample 2	KE1450	Kenaf	1450 g/mm^2	2.15 mm	674 g/mm^3
Sample 3	KE1450	Kenaf	1450 g/mm^2	1.6 mm	906 g/mm^3

3.2 X-ray computer tomography aided engineering

This section describes the X-ray computer tomography aided engineering process and how it has been interpreted in this thesis project. An illustrative schematic for the XAE process is shown in Figure 3.3 below where each part of the process will be further discussed in this section. The presented XAE process is based on the methodology presented by Auenhammer and co-authors [2] with some modifications. Initially, the methodology presented by Auenhammer and co-authors is tested and compared with available commercial software. After comparison, it was concluded that the most preferable tool for the XAE process is the commercial software RETOMO by BETA CAE, which is used throughout the following section.

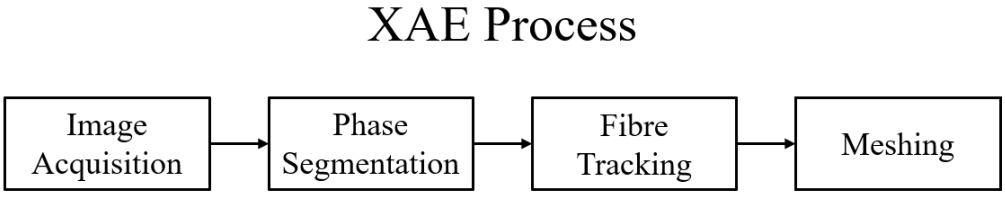

Figure 3.3: X-ray computed tomography aided engineering and its core elements.

3.2.1 Image Acquisition

The X-ray computer tomography scans were performed on a Zeiss Xradia Versa 410 scanner at Technical University of Denmark (DTU) Imaging Centre in Lyngby, Denmark. In Figure 3.4, the inside of the scanner is shown. The scanner consists of four main parts: an X-ray source, a detector, a sample holder and a camera. The X-ray source sends beams of X-ray towards the sample and the different phases inside the material reflects different amount of X-ray. This enables the separation of different phases inside the sample, which is the main interest of the scanning procedure.

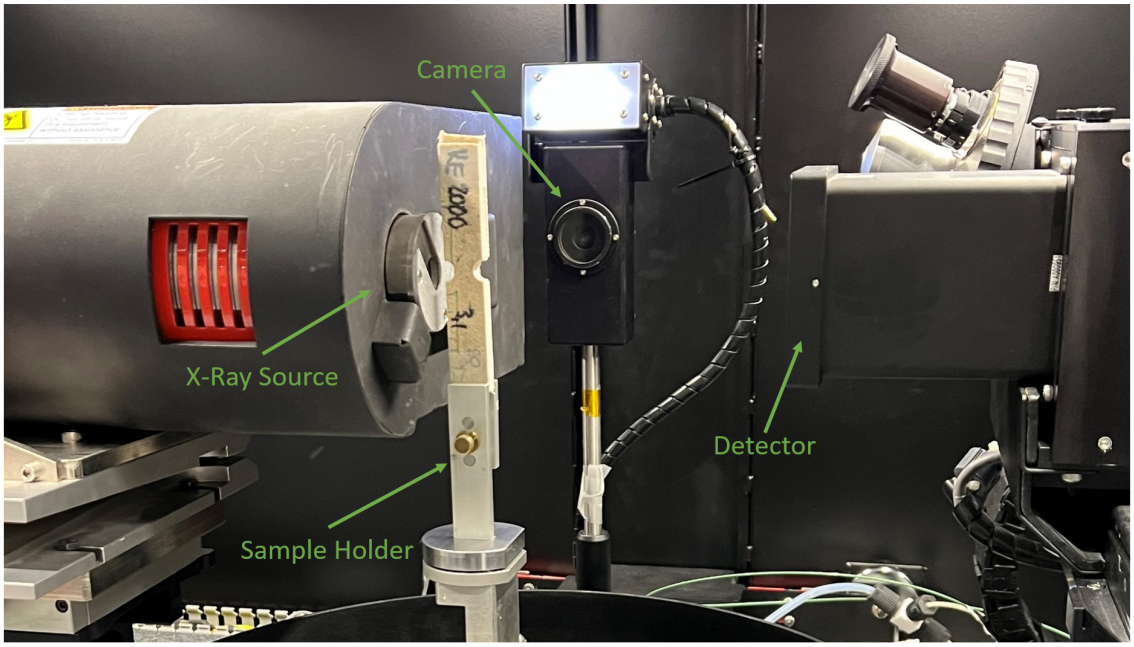

Figure 3.4: Zeiss Xradia Versa 410 scanner at DTU Imaging in Lyngby, Denmark.

Three samples are stacked together to lower the total number of scans from 9 to 3 scans with 3 samples per scan. The stacks contain three samples from the same mat, i.e. all three samples in the stack have the same aerial weight, thickness and density. Two of the samples are loaded in tension prior to scanning, one to 80% of the expected strength and the other one is loaded until failure. In this thesis, the main interest lies in the undamaged sample, which will later be simulated. With a pixel size of 8 μm, it is possible to capture the entire field of interest, see Figure 3.5 for field of view marked with a red box. To get a clear image where it is possible to distinguish the difference between void, matrix and fibre, 3601 projections are generated using an exposure time of 10 seconds.

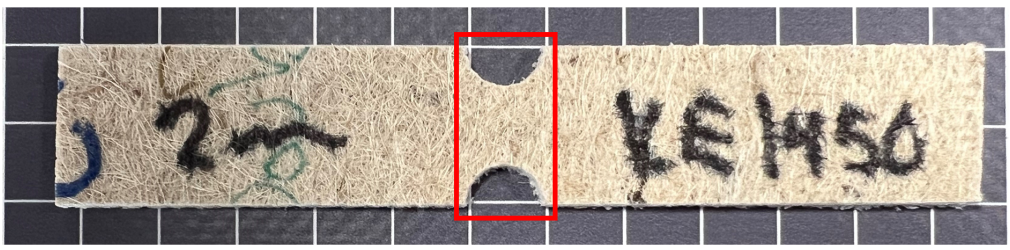

Figure 3.5: Sample 2 where the field of view for the scanner is marked by the red square.

The result from the image acquisition is a reconstructed grey-scale image where it is possible to separate void, matrix and fibres from each other. To generate the reconstructed image from the acquired image data a reconstruction algorithm is used. An example of how such a reconstructed image can look is presented in Figure 3.6.

From the figure, it is be noted that the contrast is varying over the entirety of the image. If one were to compare fibres along the edges with fibres in the centre of the image it is clear that the considered fibres will have different grey-scale values meaning that the segmentation will be challenging. This contrast issue is due to the intensity of the CT scanner as the intensity is at its highest in the centre of the image and gradually decreases away from the centre. To overcome this issue the image is cropped where the notches start and end, similar to the red box drawn in Figure 3.5.

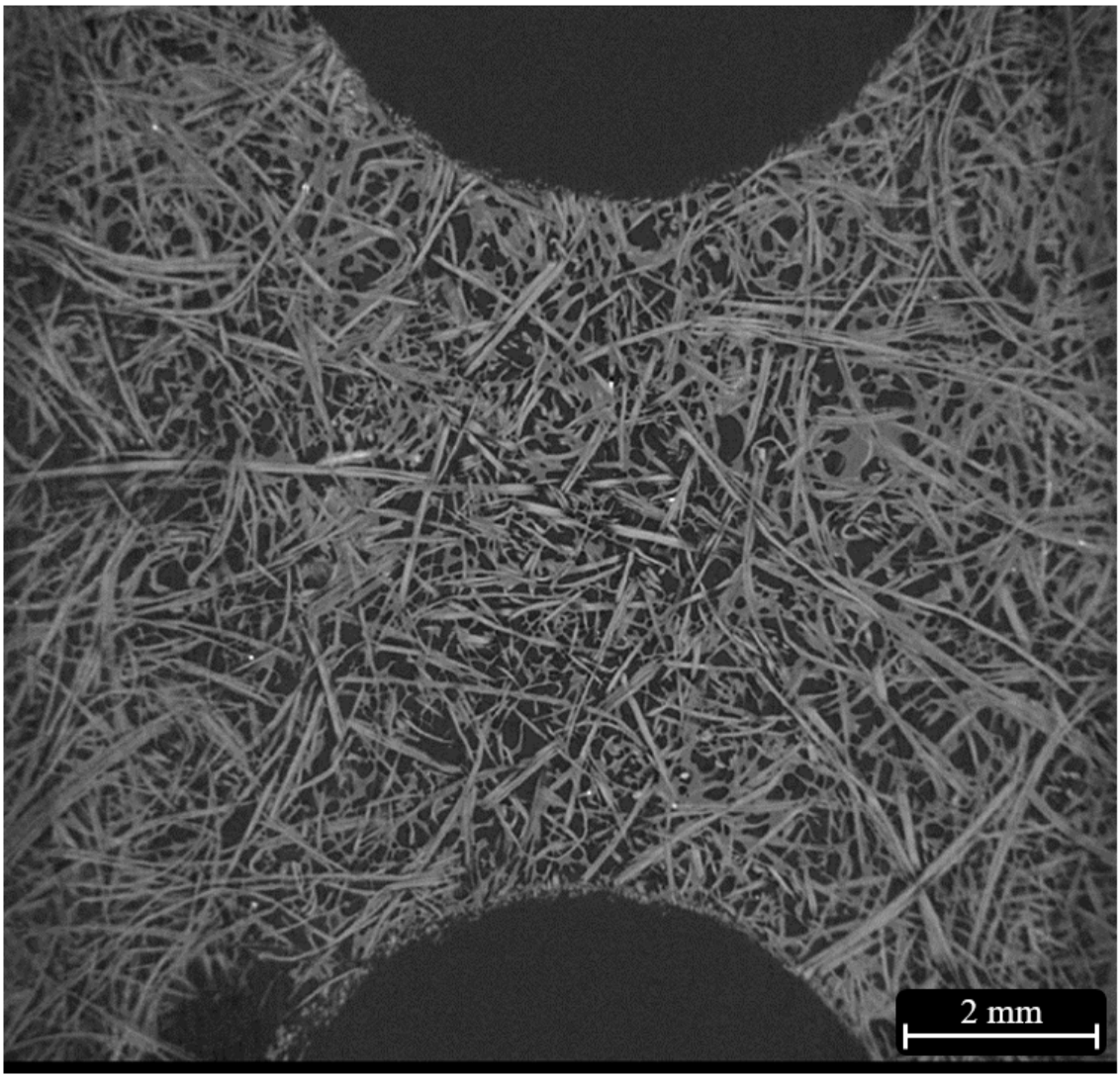

Figure 3.6: An example of a reconstructed image where the intensity issue along the edges can be observed.

3.2.2 Phase Segmentation

Phase segmentation and meshing are performed using the commercial software RETOMO from BETA CAE Systems. The required input file for the analysis in RETOMO is in .raw format meaning that the acquired scan file (.txm format) needs to be converted. This is done by some modifications of a Python script provided by Jeppesen and co-authors [22]. This segmentation procedure is needed to model the different phases void, matrix and fibre as three separate materials. The segmentation is made with a threshold method, as described in Section 2.3. To obtain a difference between the phases two threshold values need to be determined, one for the threshold of the grey-scale value between void and matrix and one between matrix and fibre. As the fibre and the matrix have similar densities this segmentation procedure is challenging. To get reasonable initial guesses of the volume fractions of the three phases an analytical distribution is obtained. To obtain these analytical values an assumption is made. It is assumed that the fibre density is 1.4 g/cm^3 and matrix density is 0.9 g/cm^3. With this assumption, together with the 50-50 weight ratio between matrix and fibre, the volumetric distribution is computed according to standard [23] and presented in Table 3.2.

Table 3.2: Analytical volume fractions of void, matrix and fibre.

	Void [%]	Matrix [%]	Fibre [%]
Sample 1	45.1	34.1	20.8
Sample 2	38.3	38.3	23.4
Sample 3	27.4	45.1	27.5

Once the void, matrix and fibre fractions are obtained an iterative process to find the grey-scale thresholds are performed. This iterative procedure includes threshold management and mesh creation, where the main target is to reach similar fractions as in the analytical computation. One big advantage of the commercial software RETOMO is that during the segmentation stage, it is possible to drag the thresholds along the histogram in real-time. This enables quick changes in the thresholds leading to a decreased time in the segmentation process. An image of how the fibres are captured in real-time is presented in Figure 3.7.

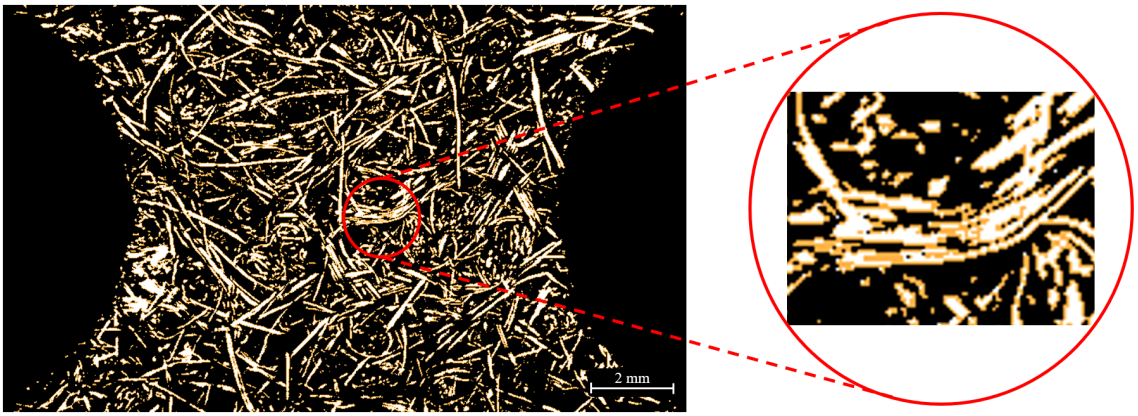

Figure 3.7: The fibre threshold value can be determined while changing the grey-scale values in real-time. The white parts are fibres and the orange lines marked the areas that are currently included in the segmentation given the chosen threshold value. When a desired threshold value is obtained all fibres should be enclosed by an orange boundary.

3.2.3 Fibre Tracking

The fibre orientation information from the scanned image is of interest in the analysis. This information can be obtained by the "Fibre Tracking" tool in RETOMO. The method of finding the orientations is a process where a number of assumptions need to be made. These assumptions are verified and presented in a parameter study, see Appendices A.1 and A.2.

The first step is the template matching where the orientation is determined in each pixel of the image. To run this template matching a couple of settings are needed, dimensions of the fibres such as cylinder radius, cylinder length and mask radius as well as an angular search increment are needed. A good estimate is to set the length and radius to a value where most fibres fit. It is important that the cylinder length is short enough to capture all curved fibres. The mask radius is a measure of a small layer of matrix material surrounding the fibre. These three values will remain constant throughout the template-matching procedure. Then the program will find the angles in which the fibres are oriented. The other value that is fixed and should be defined is the angular search increment which describes the angular increment for the fibre tracking. This angular search increment will be studied closer during a parameter study later on, see Appendix A.2 for the parameter study. The result of the template matching is a correlation value between 0 and 1 for each pixel. An example of these correlation values can be observed in Figure 3.8. The correlation value stands for how well the cylinder matches the intensities of the scanned image.

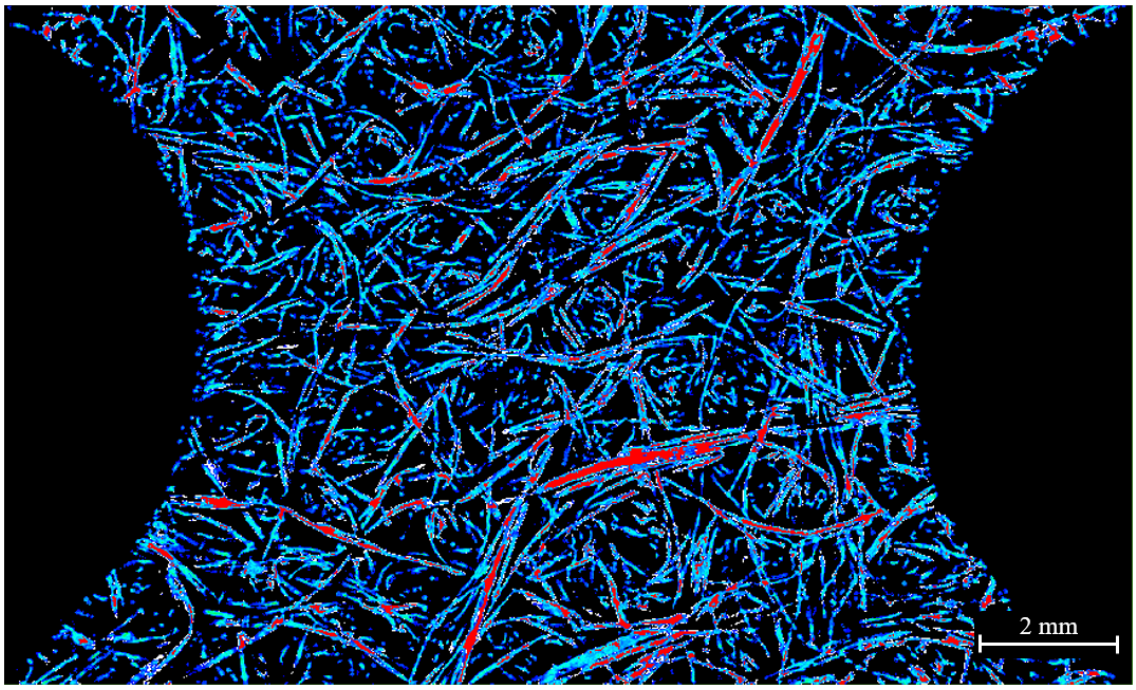

Figure 3.8: Correlation values for the fibres, red represents 1 dark blue is equal to 0. The correlation value 1 stands for good correlation and 0 stands for poor correlation.

Apart from the correlation values, it is also possible to study the computed orientations at this stage. The next step is to do the tracking of the fibres. The fibre tracking procedure is based on the correlation values mentioned earlier. To detect the fibres two threshold values need to be defined as the "fibre seed value" and the "fibre propagation value". These values should be picked so that all fibres are detected and that there is a maximum value that the fibre will propagate towards. This can be studied graphically in RETOMO, as illustrated in Figure 3.9.

Figure 3.9: Image showing the fibre seed value (orange) and the fibre propagation value (blue). Black parts are void and matrix whereas the white parts are fibres, from RETOMO.

The tool will start by defining a fibre within the orange lines and let the fibre propagate towards the blue line surrounding the fibre. In this process, the neighbouring pixels are

taken into account and the neighbours that are matrix or void will not be included in the fibre tracking. Once these settings are in place one can create the fibre orientation information and gather all fibres as a cluster.

3.2.4 Meshing

In RETOMO, one can choose to mesh with surfaces or solids. In this thesis, a mesh of solid elements is used. There is a function in RETOMO called "Voxels to Hexas" which makes solid hexahedron elements from the pixel information of the image. One will have to determine how many pixels should be sub-sampled into one hexahedron and by this determine the element size. A sub-sampling rate of 5 was used in this work meaning that $5 \times 5 \times 5 = 125$ pixels will be formed into one solid element as shown in Figure 3.10 below. The phase of the element is determined by the most frequent phase among all pixels in the element. With a pixel size of 8 μm and a sub-sampling rate of 5, the element size is 5×8 μm $= 40$ μm. To ensure that the selection of sub-sampling rate does not affect the final results, a parameter study is made and presented in Appendix A.1.

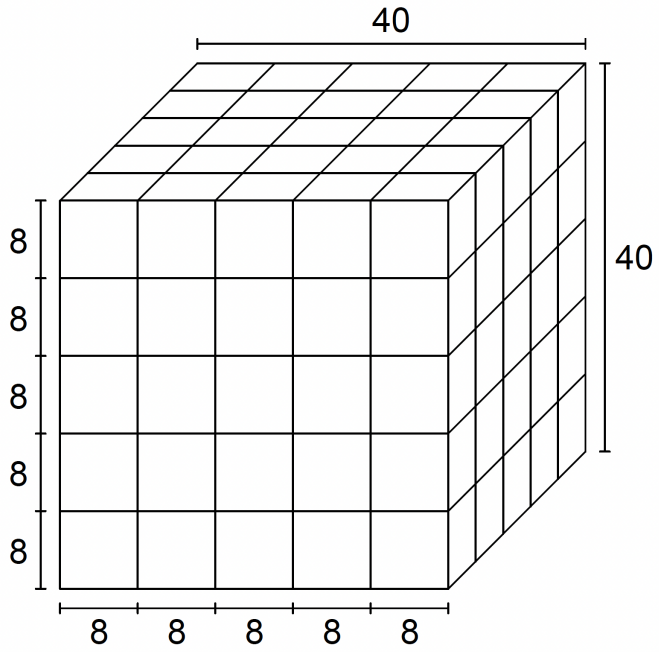

Figure 3.10: Hexahedron element where $5 \times 5 \times 5$ pixels is sub-sampled into one element. The length unit is μm.

3.3 Mechanical tests

The mechanical tests are performed in the lab at Volvo Cars Material Centre in Torslanda. To perform the tests a MTS Criterion model 45 machine is used with the GOM Aramis 3D 12M system for DIC analysis. The MTS machine is equipped with the MTS Advantage Wedge Grips to hold the sample in place during the test. The Aramis setup is presented in Figure 3.11 below. The distance between the grips is 50 mm and the sample is pulled axially with a strain rate of 50 mm/min until failure and the load cell size is 100 kN.

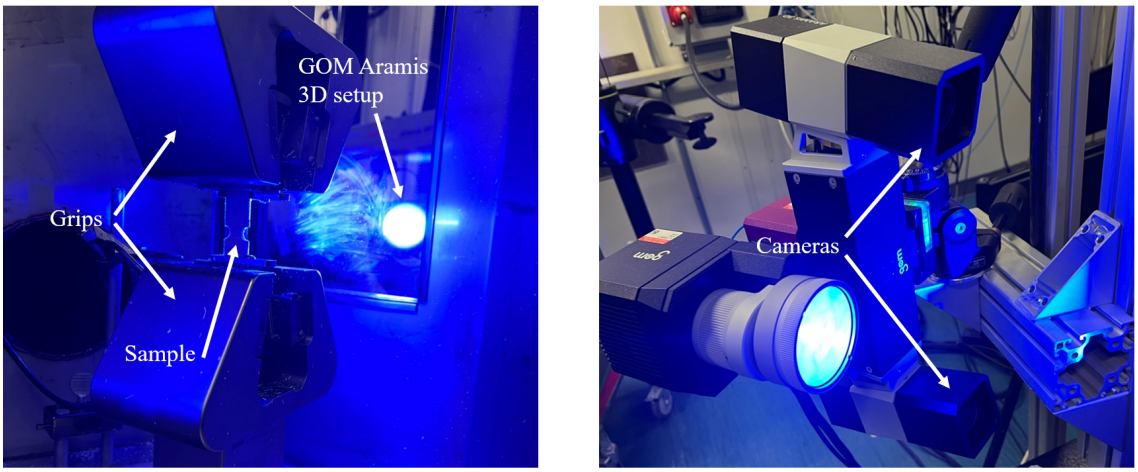

Figure 3.11: The mechanical test setup where the leftmost figure shows the grips that keep the sample in position. The rightmost figure shows the GOM Aramis 3D 12M system used for the DIC data gathering.

3.3.1 Digital Image Correlation (DIC)

The DIC data is gathered with the GOM Aramis 3D 12M system as explained earlier. From this analysis, it is possible to plot the surface of the sample. In addition to the surface, two curves are defined to enable measurements of the average displacements between these two curves. An example of such a surface is presented in Figure 3.12. From the figure, it is noted that the displacements are not constant over the curves. Therefore, it is important that the average displacement over the curves is considered moving forward. This is important for the simulations at a later stage.

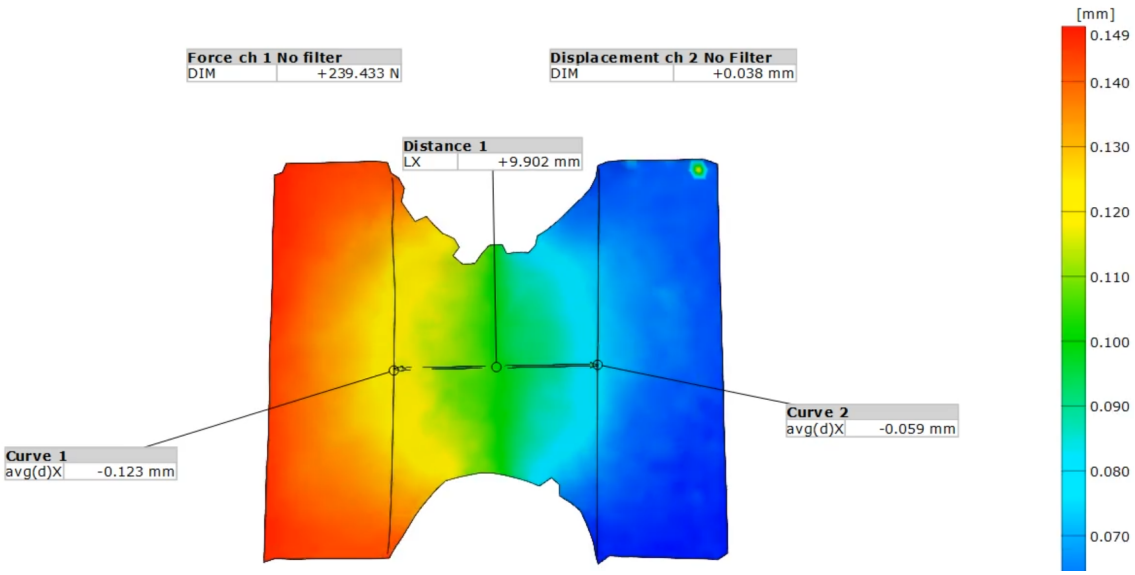

Figure 3.12: The result from a DIC is shown where the displacements on the surface is visible.

3.3.2 Microscopy

Both prior to and after testing all samples will be analysed in an optical microscope. Prior to testing the microstructure will be analysed where the main focus lies on how the matrix is affected by different amount of pressure during manufacturing. How well the fibres are embedded in the matrix is another interesting topic to examine prior to testing. After the physical tensile test, the samples will be analysed in the fracture surface. The most interesting aspects in analysing the fracture surface are how the fibres or matrix have fractured and what physics that can be observed. It is essential to understand the fracture physics as the need to be reflected in the model in the damage analysis later on.

3.4 Finite Element Model

The finite element model is established using the mesh, phase and orientation information from the XAE process. As the mesh is generated from a scanned image of a physical coupon the double notch is not perfectly symmetric. In order to exclude possible errors and have a more reliable model the exported mesh is cleaned. Elements are removed in the notched region creating a geometrical symmetric model without noise. The procedure is illustrated in Figure 3.13.

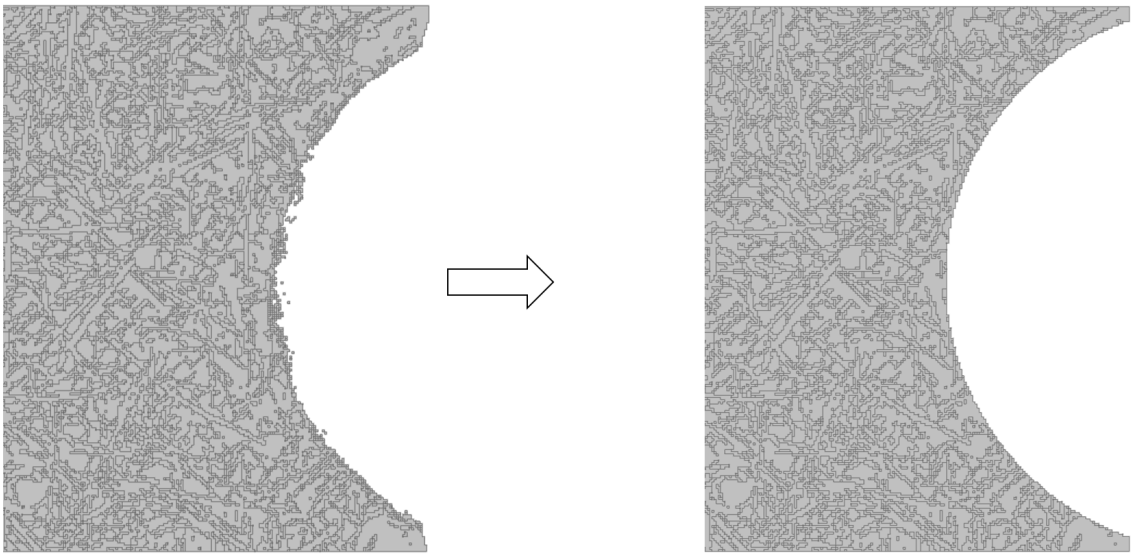

Figure 3.13: Both the old and the cleaned mesh from the commercial pre-processor ANSA by BETA CAE Systems.

The number of elements are spanning from 2 million to 5 million depending on the sample. With respect to the large amount of elements and the computational time a simple element formulation is desired. Therefore, a hexahedron element with 8 nodes is chosen and used in all simulations. Independent of which phase an element belongs to, all adjacent elements share nodes and are therefore linked together.

3.4.1 Boundary Condition and Load

The finite element model represents a small portion of the physical double notch coupon and the boundary condition should represent a continuous structure. Therefore, the boundary conditions should not restrain the contraction of the cross-sectional area and induce unrealistic stress concentrations. Considering the geometry of the model the stress should concentrate in the centre where the cross-sectional area is the smallest. However, this will also depend on the microstructure and the stress will not be uniformly distributed in the physical coupon or the simulation. In order to fulfil this and not induce unrealistic boundary effects only the x-translation is fixed along the boundary.

The load is applied by uniformly ramping the velocity of the displacement along the opposite boundary according to Figure 3.14. The velocity is increasing linearly in the beginning to prevent oscillations. As mentioned in Section 2.6 one cannot simulate the same loading rate as in the physical test due to computational time. The ratio between internal and kinetic energy should be monitored to ensure quasi-static conditions throughout the simulation. The loading rate is illustrated in Figure 3.14, which is used for all simulations after careful consideration of the energy balance.

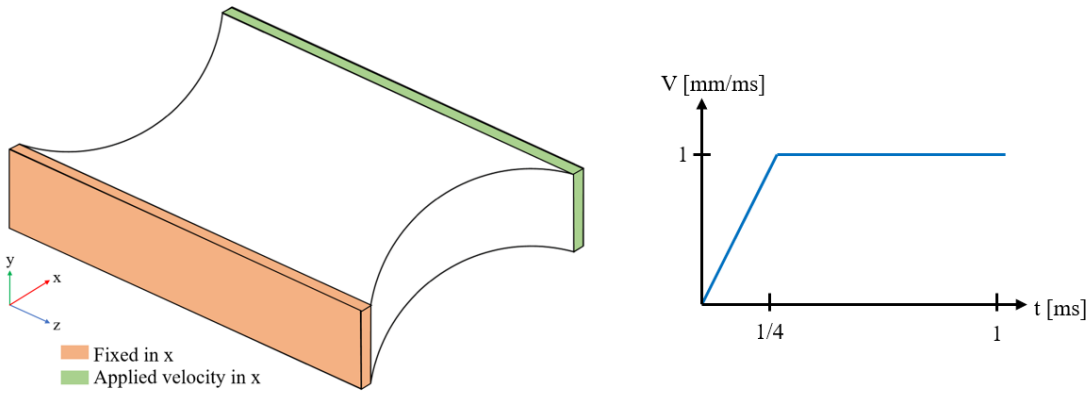

Figure 3.14: Illustration of the boundary condition and loading in the leftmost image. To the right, the evolution of the displacement over time is presented.

3.4.2 Modelling of Voids

From the scanned image and phase segmentation it is clear there are a substantial amount of voids in the structure. Therefore, it is investigated how the voids should be modelled. The voids can either be meshed and included in the model or excluded. If the voids are meshed the problem appears which material parameters one shall apply without changing the characteristics of the composite. On the other hand, excluding the voids creates big hollow structures inside the mesh which lead to instability and numerical issues. Therefore, the voids were meshed and given similar material properties as the matrix, but a stiffness low enough not to affect the global behaviour. In Table 3.3 one can see how the relative coupon stiffness change depending on the voids stiffness.

Table 3.3: Void stiffness versus normalised coupon stiffness.

Void stiffness [MPa]	10	1	0.1	0.01
Normalised coupon stiffness [-]	1	0.973	0.969	0.965

The change in coupon stiffness is small in comparison to the change in void stiffness. A higher voids stiffness resulted in a more stable simulation. Hence, the void stiffness was chosen to 10 MPa.

3.5 Material modelling

A specific material model is applied to each phase giving a complex highly non-uniform stress state. Due to the complexity of the microstructure, the material modelling and calibration are divided into steps where one characteristic of the response is added at a time and calibrated individually. The material properties of the constituents are unknown and a first guess is made from literature, see Table 2.1 in Section 2.2. In order to calibrate the material models the simulated engineering stress-strain curve is compared against the mechanical test curve.

3.5.1 Elasticity

In the simplest case, both matrix and fibres have an elastic material model. The simulated stress-strain curve is compared against the elastic region of the mechanical curve. The elastic region is defined by data from 0 to 0.25% strain. The calibration of the constituents is done manually by changing the material properties and establishing a range which results in a correct curve match. Furthermore, the calibration process has been limited to the stiffness variables of the fibre and matrix. The impact of Poisson's ratio on the coupon stiffness will be further investigated in a parameter study, see Appendix A.3.

3.5.2 Orthotropy

Due to the complex microstructure of natural fibres, e.g. hollowness, it is a given choice to assume orthotropic material behaviour. In order to limit the amount of free variables in the calibration procedure a relation between the stiffness parameters is established. Research from Karakoc et al. on cellulose fibres [4] have been utilised in order to establish the relation between the parameters. The material model used in LS-Dyna is *MAT_ORTHOTROPIC_ELASTIC* which include the following parameters: E_x^f, E_y^f, E_z^f, G_{xy}^f, G_{xz}^f, G_{yz}^f, ν_{xy}^f, ν_{xz}^f and ν_{yz}^f. Due to the lack of information all stiffness parameters depend linearly on the longitudinal stiffness E_x^f following the ratio Karakoc et al. used [4] as follows:

$$E_x^f \text{ Calibrated} \qquad E_y^f = E_z^f = \frac{E_x^f}{19.52/5.5}$$
$$G_{xy}^f = G_{xz}^f = \frac{E_x^f}{19.52/4.5} \qquad G_{yz}^f = \frac{E_x^f}{19.52/1.5}$$
$$\nu_{yz}^f = 0.35 \qquad \nu_{xy}^f = \nu_{xz}^f = \frac{\nu_{yz}^f}{0.39/0.07}$$

As the assumptions mentioned earlier are based on another type of fibre the results will not be trustworthy to elaborate further on. As there is a lack of information about the fibres, considered in this thesis, it will only be investigated if implementing the fibre orientations and an orthotropic fibre model will provide benefits compared to isotropic fibres.

3.5.3 Plasticity

In this section plasticity is introduced on the matrix by using the material model *MAT_PIECEWISE_LINEAR_PLASTICITY* which are presented in Section 2.5.1. The fibres are modelled using an elastic isotropic material model as in Section 3.5.1. A first guess of the plasticity parameters are based on a previously calibrated flow curve for a common polypropylene shown in Figure 4.15. In order to calibrate the stress-strain curve, the plasticity flow curve is scaled using a scaling factor, σ_{sf}, which inserted in Equation 2.1 results in Equation 3.1. The scaling of the flow curve is presented in Figure 3.15.

$$\phi = \sigma_{vM} - \sigma_{sf} \cdot \sigma_y \tag{3.1}$$

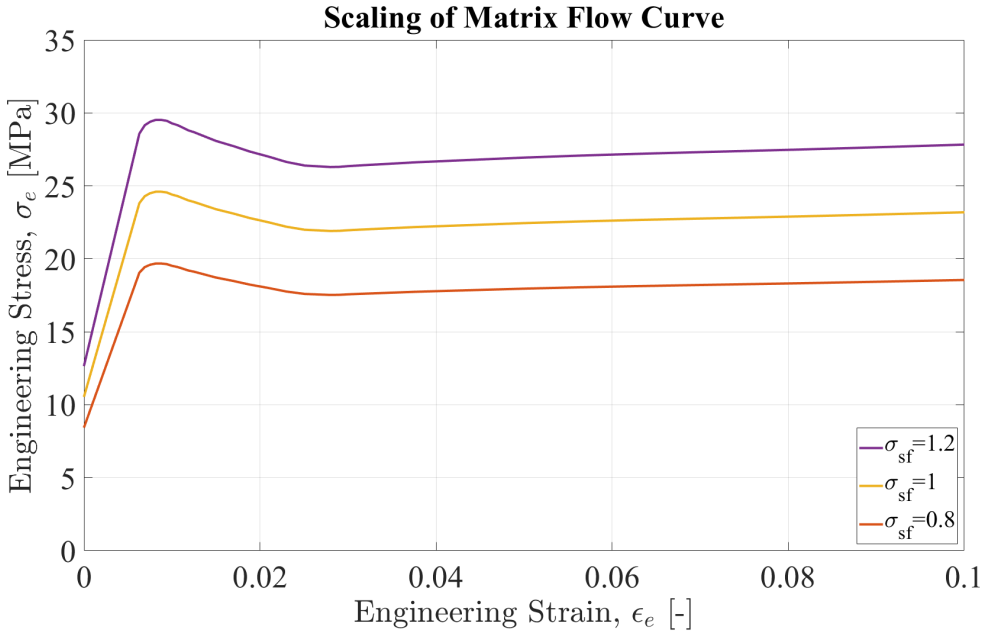

Figure 3.15: Flow curve used in the plasticity model and how it is scaled. σ_{sf} represent the scale factor of the flow curve. The curve extend beyond the limits in the plot.

3.5.4 Damage and failure

A brittle fibre failure is implemented in the model to capture the peak load from the mechanical test. The damage is implemented on the fibre elements using the *MAT_ADD_EROSION* card as introduced in Section 2.5.2. The fibre elements are deleted if the strain exceeds the ultimate principal strain, ε_{fU}. The peak load is calibrated by changing ε_{fU} so the simulated peak load matches the mechanical test response. A schematic image of the fibre stress-strain response is shown in Figure 3.16.

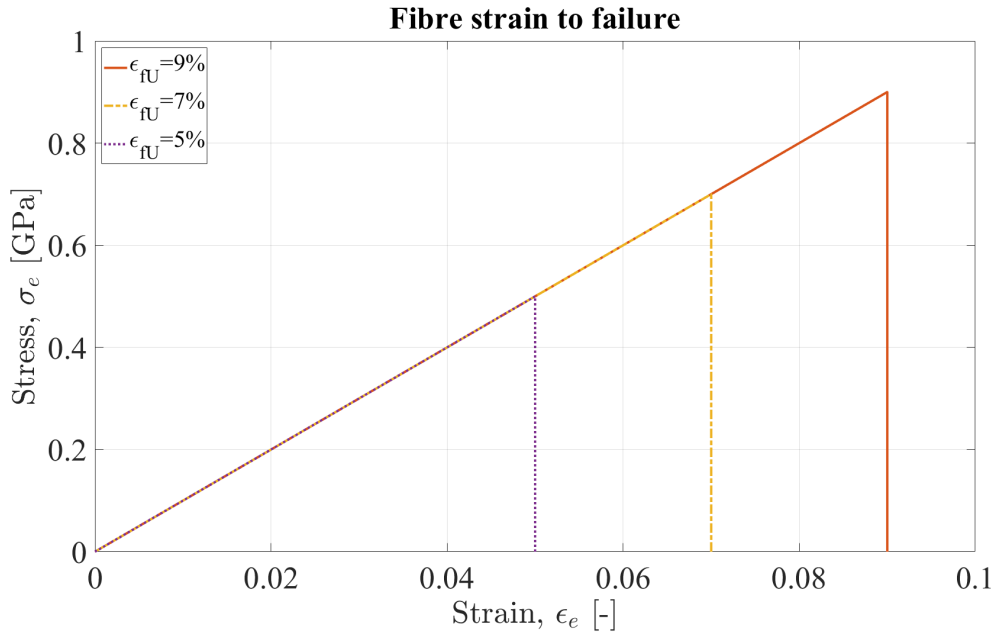

Figure 3.16: Stress-strain response of the fibre elements. ε_{fU} is the ultimate fibre strain.

4

Results

4.1 XAE results

In the XAE stage of the project, a number of milestones are fulfilled and those will be presented in the following section. The results that are presented from the XAE process are a reconstructed image from the image acquisition, a histogram of the grey-scale image data, a figure showing the phase segmentation, an image of the mesh, a table of volume fractions and an image where the fibre orientations are visible. The results from the XAE methodology for Sample 1 are presented in this section. The results for Samples 2 and 3 is presented in Appendix B to avoid repetitive results in the following section.

A reconstructed image of Sample 1 is presented in Figure 4.1 below. In the figure, it is observed that the scan of the sample has been cropped as explained in Section 3.2.1. The scan time of the bundle was approximately 12 hours and the image data (.txm file) file size was 16.4 GB.

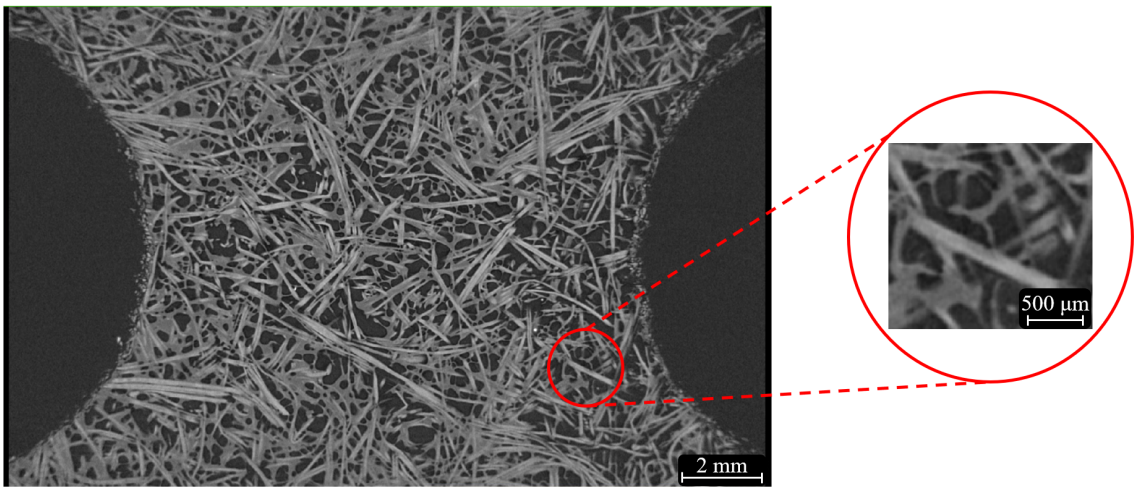

Figure 4.1: Reconstructed image of Sample 1. Images are from the commercial software RETOMO.

The grey-scale threshold for void - matrix is 2300 and the threshold for matrix - fibre is 2900. The grey-scale values are collected in a histogram, presented in Figure 4.2 below.

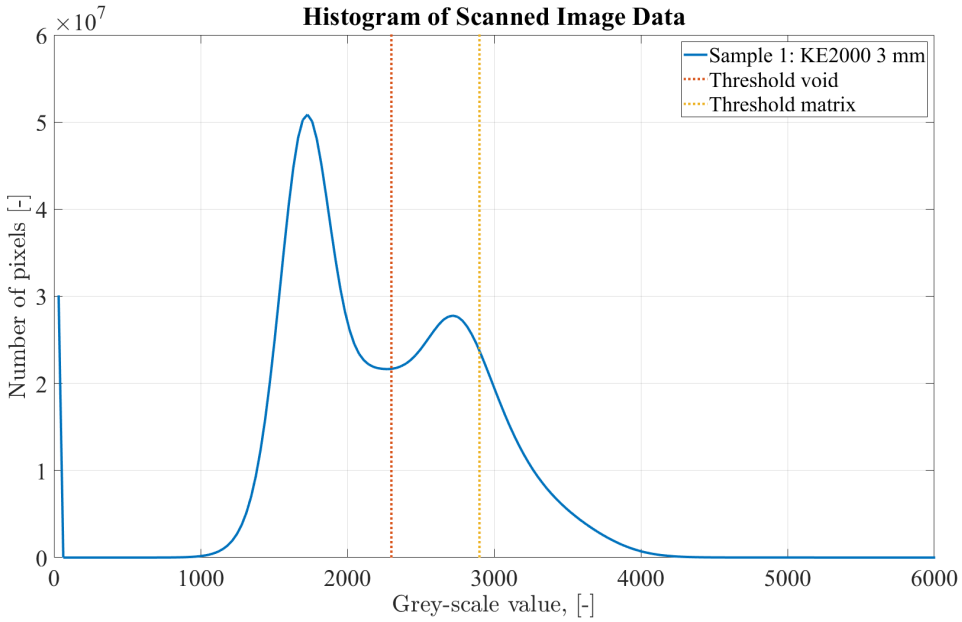

Figure 4.2: Histogram of the grey-scale image data from the image acquisition for Sample 1.

The phase segmentation is presented in Figure 4.3 where the three phases void, matrix and fibre are indicated by three different colours. The blue parts are surrounding air and voids inside the composite, the red parts are matrix and the yellow are fibres. This phase segmentation is gained from the threshold values presented in the previous paragraph.

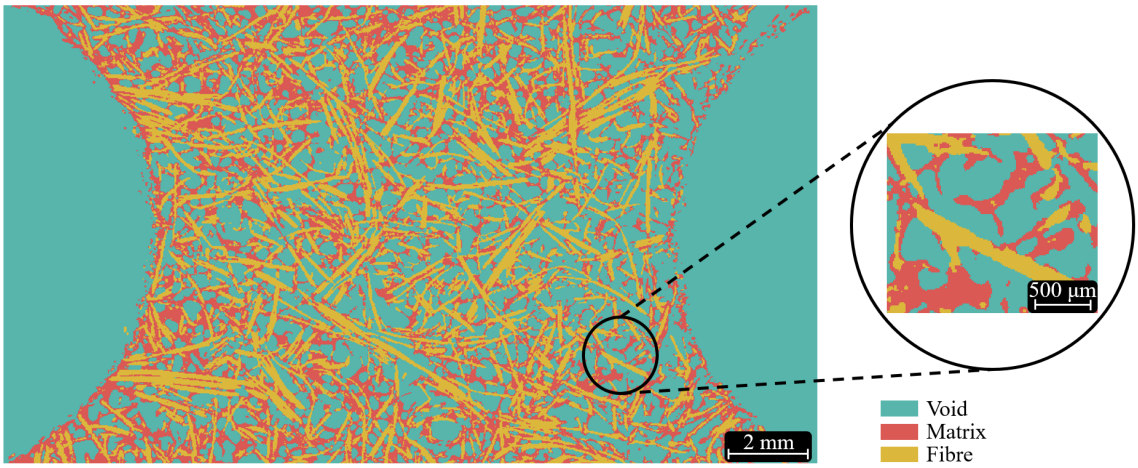

Figure 4.3: Segmentation of the three phases void, matrix and fibre for Sample 1.

The generated mesh is presented in Figure 4.4 where each phase is presented with a unique colour. The voids inside the composite are the black parts, the matrix material is the grey parts and the fibres are white. With a sub-sampling rate of 5, the model has 4,757,826 8-noded hexahedron elements.

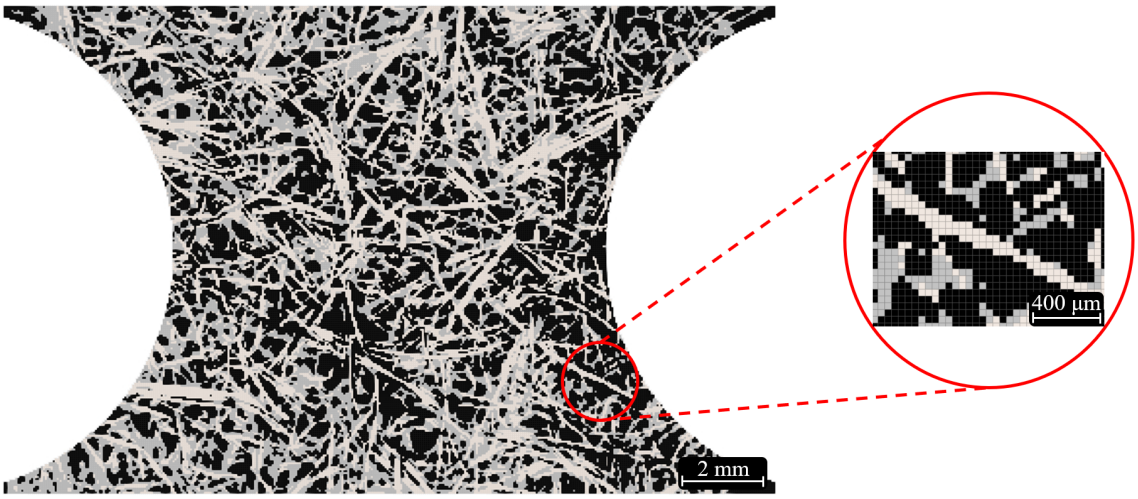

Figure 4.4: The generated mesh for Sample 1. The total number of elements is 4,757,826.

The volume fractions of void, matrix and fibre are presented in Table 4.1. From this table it is observed that the void volume fraction is 2.7% higher in the simulation compared to the analytical value. Further, it is noted that the matrix fraction is 4.0% lower and the fibre fraction 1.0% higher compared to the analytical volume fractions. These differences comes mainly from the clean-up procedure described in Section 3.4 but as the deviation is within 5% it is accepted.

Table 4.1: Comparison of simulated and analytical volume fractions of void, matrix and fibre for Sample 1.

	Void [%]	Matrix [%]	Fibre [%]
Analytical	45.1	34.1	20.8
FE Simulation	46.3	32.8	21.0

To study the results from the fibre tracking described in Section 3.2.3 an image, where the element orientations are visible, is presented in Figure 4.5. The image is the same cut-out as presented in the rightmost part of Figure 4.4 where a fraction of a fibre is cut out in order for the orientations to be visible. The red arrows indicate the direction of the fibre along the global x-axis. The presented orientations are in line with the expected fibre direction from the microstructure.

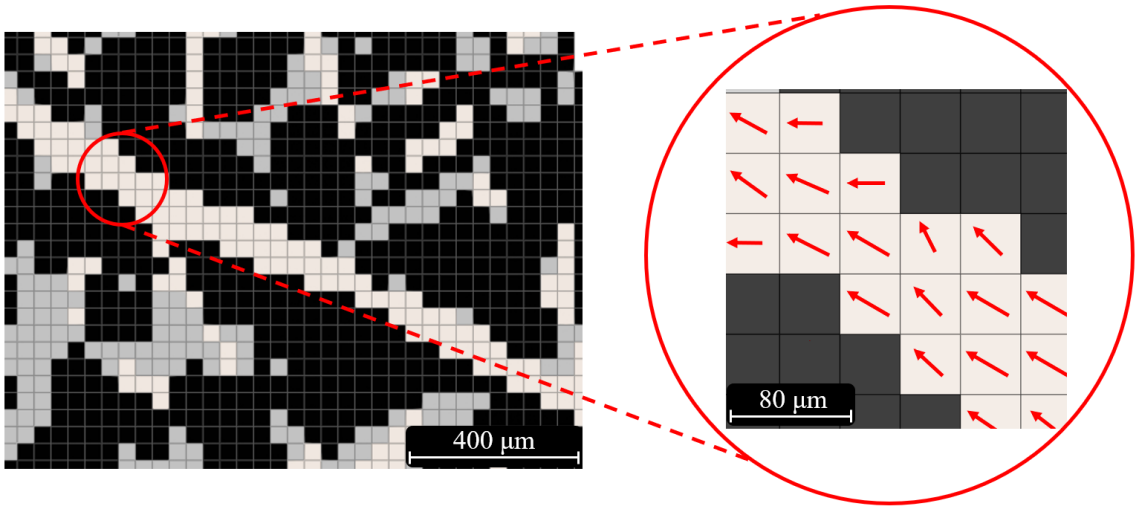

Figure 4.5: Fibre orientations are visible for each element in sample 1. The red arrows indicate the direction along the global x-axis.

4.2 Mechanical test results

The mechanical tests have been performed as described in Section 3.3. In this section the results from these tests are presented. In Figure 4.6 the stress-strain response for all three samples are presented. From this figure it is observed that Sample 1 and Sample 2, that have similar densities, show similarities in the overall behaviour whereas Sample 3 show a different behaviour.

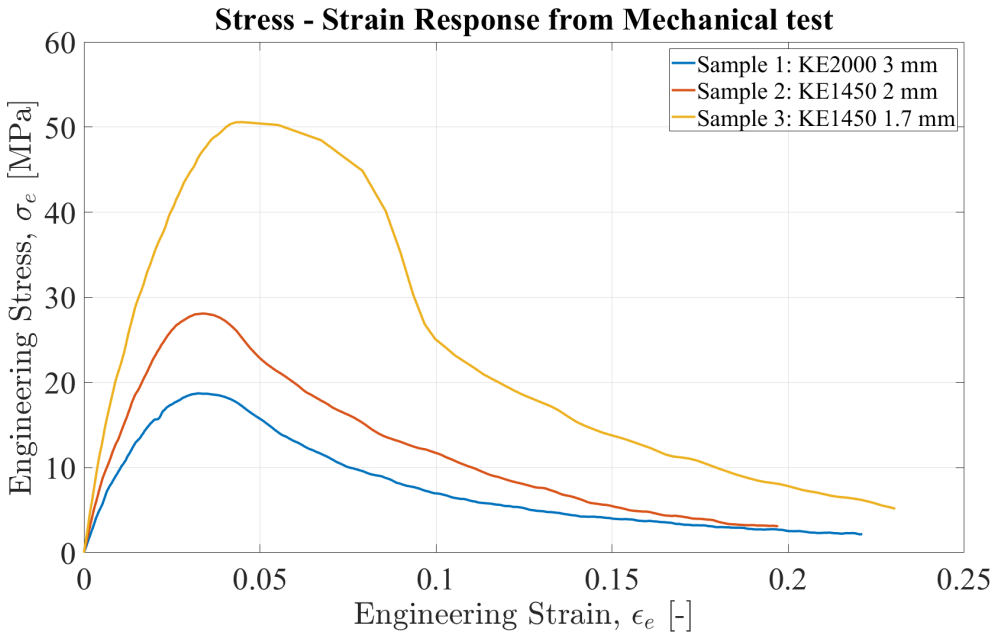

Figure 4.6: Stress - strain response for all three samples from the mechanical tensile test.

Further, the failure modes of all three samples are presented in Figure 4.7. From the

figure it is noted that Sample 1 and Sample 2 have a straight fracture surface whereas Sample 3 has an angular fracture. The angular fracture and the different behaviour in the stress-strain response, Sample 3 indicate that other mechanical characteristics govern the material behaviour.

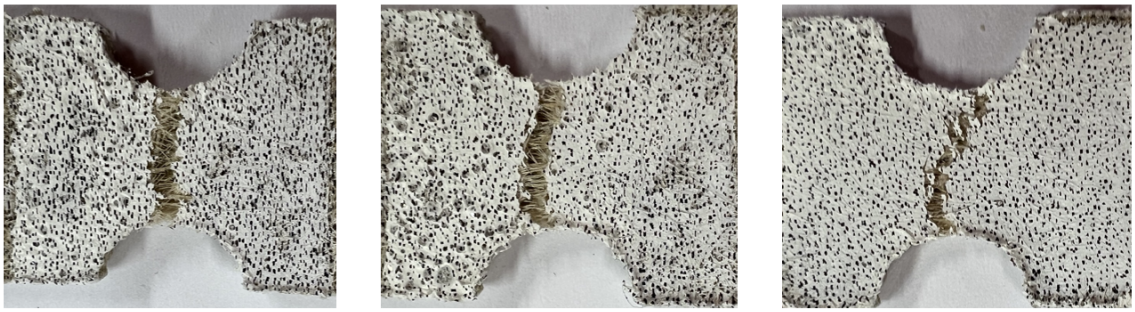

Sample 1: KE2000 3mm | Sample 2: KE1450 2mm | Sample 3: KE1450 1.7mm

Figure 4.7: Failure modes for all three samples from the mechanical tensile test.

4.3 Microscopy

Both prior to and after testing, the samples are analysed in a optical microscope. Two aspects are investigated and presented in this section. Firstly, an investigation on how the varying amount of pressure in the manufacturing is affecting the microstructure is performed. Then after the physical tests the fibres in the fracture surface are analysed.

Figures 4.8 - 4.10 shows the microstructure of three different samples. The first one, Figure 4.8, is an unpressed mat where both kenaf and PP fibres are visible. In Figure 4.9 the microstructure of Sample 1, which is pressed to a thickness of 3 mm, is presented. In the figure it is observed that as the mat has been pressed the matrix has melted and embedded the fibres. From Table 4.1 we remember that the analytical and simulated volume fraction of voids is approximately 46%. With this is mind when observing the microstructure in Figure 4.9 it is noted that there is a considerable amount of voids which is expected from this sample. In Figure 4.10 the microstructure of Sample 3, which is pressed to 1.7 mm, is presented. It is clear that the matrix is even more smeared out and less voids is visible compared to Figure 4.9.

After testing, the fracture surface of all the samples are analysed to investigate the failure response. In Figure 4.11, a fractured fibre in the fracture surface of Sample 1 is shown. From this figure, it is observed that the fracture has a straight edge indicating that the fibre failure is a brittle tensile failure [24]. This behaviour was also observed for Sample 2 and 3.

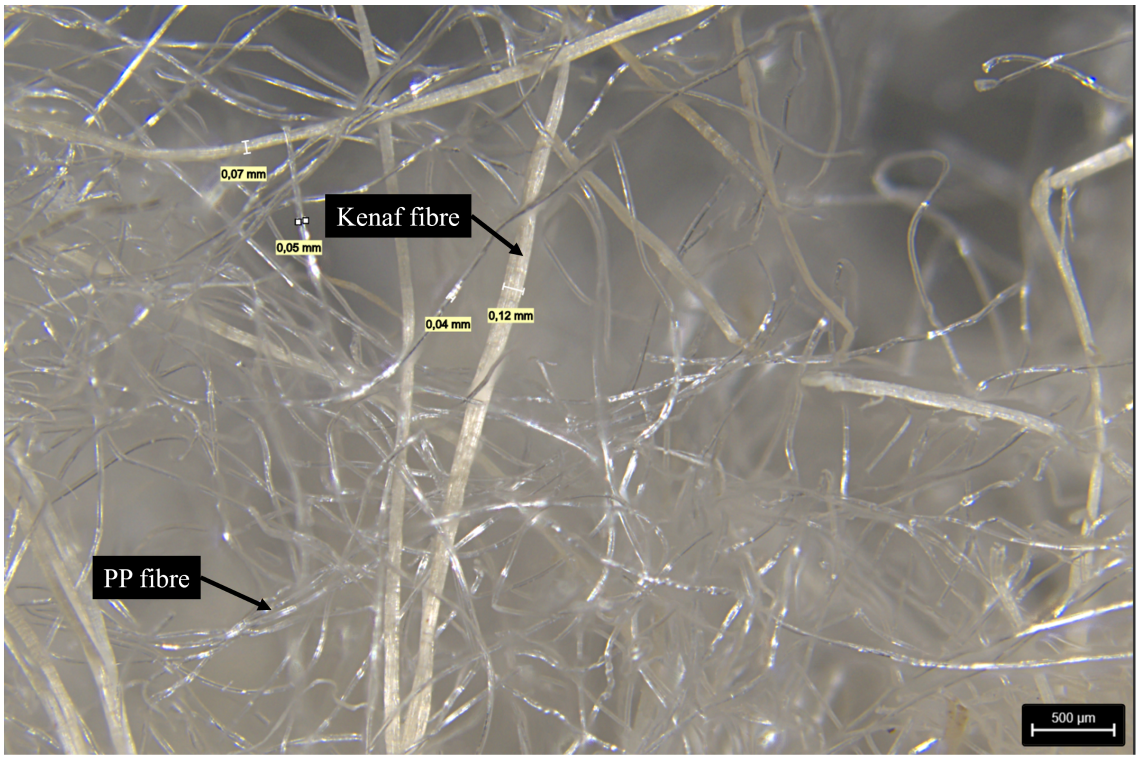

Figure 4.8: Image of the unpressed sample.

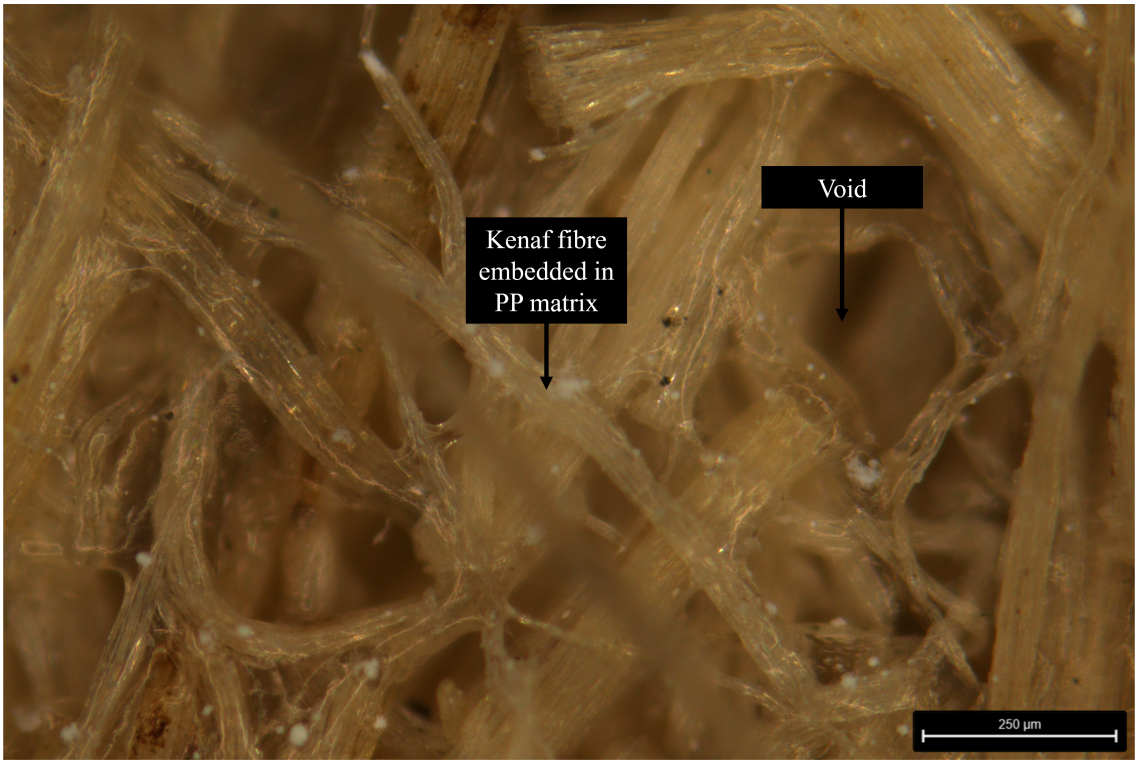

Figure 4.9: Image of Sample 1, pressed to 3 mm.

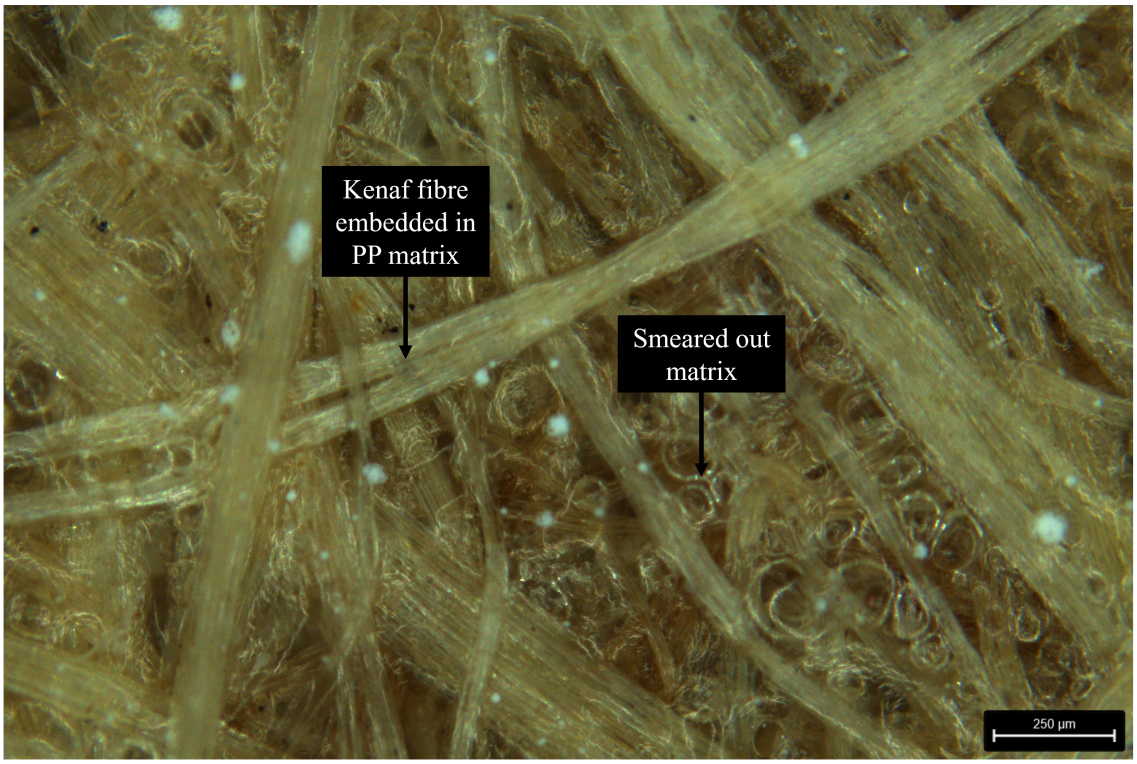

Figure 4.10: Image of Sample 3, pressed to 1.7 mm.

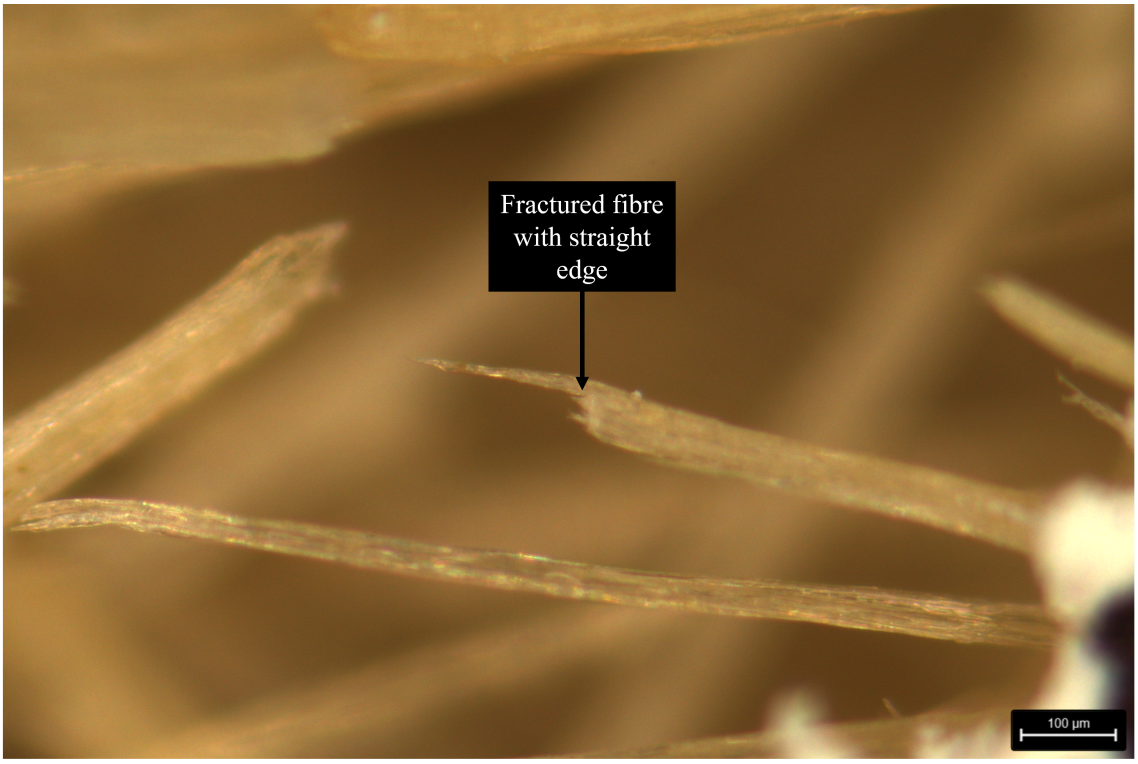

Figure 4.11: An image showing a fractured fibre.

4.4 Simulation results

The simulation results are presented with the same procedure detailed in Section 3.5. A mechanical stress-strain curve is presented together with the simulation result for each individual sample.

4.4.1 Elasticity Calibration

The mechanical properties of the constituents are unknown and calibrated within the range presented in Section 2.2 Table 2.1. The matrix stiffness has been varied between three values whereas the fibre stiffness is calibrated to match the coupon stiffness. The simulated and calibrated stress-strain response together with the mechanical test response is presented in Figure 4.12. The calibrated stiffness of the constituents and the coupon stiffness for each sample is presented in Table 4.2.

There are several combinations of constituent's stiffness properties which are giving the same coupon stiffness. Therefore a range has been defined and presented both in Table 4.2 and in a 2D line plot in Figure 4.13. The 2D line plot is generated by three data points representing the start, end and mid-point of the stiffness range for the matrix.

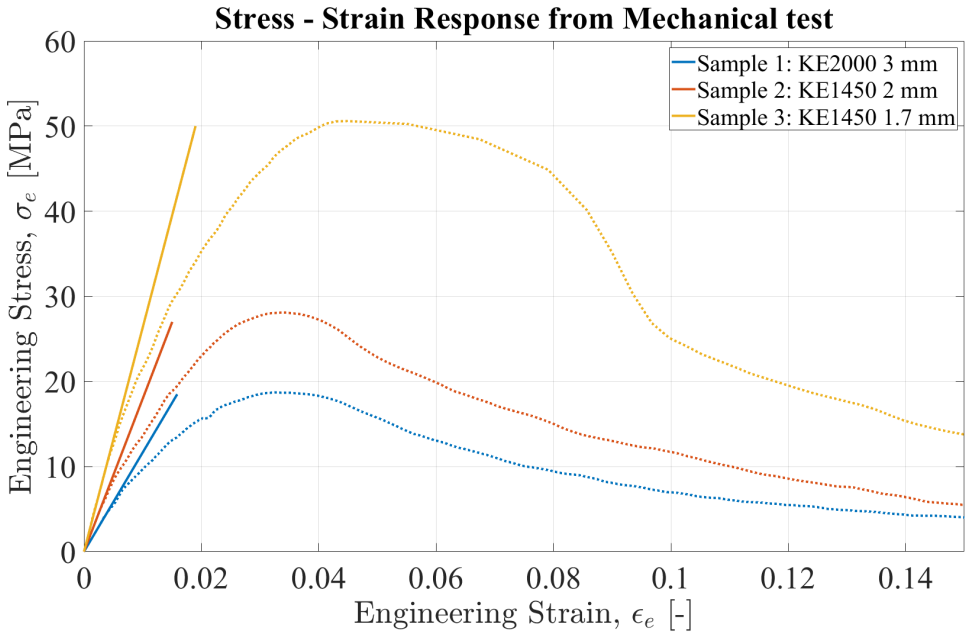

Figure 4.12: Calibrated elastic stiffness for all three samples. The dotted line repents the mechanical test and the continuous the simulation.

Table 4.2: Calibrated elastic stiffness of fibre and matrix together with the coupon stiffness.

	Sample 1	**Sample 2**	**Sample 3**
E_f [GPa]	10-17	11-20	12-25
E_m [GPa]	0.8-2	0.8-2	0.8-2
E_c [GPa]	1.16	1.79	2.63

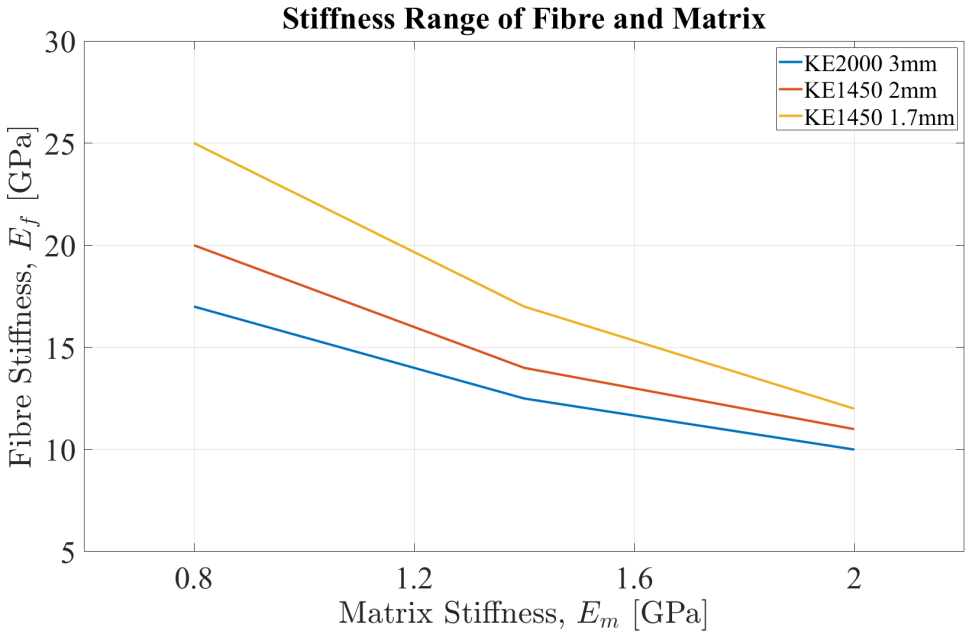

Figure 4.13: Calibrated stiffness range of matrix and fibre. Note that every curve represents one sample and its coupon stiffness.

The result from the elastic stiffness calibration shows that it is possible to calibrate the material model for all three samples within reasonable constituents stiffness properties. The range in Figure 4.13 is established from three combinations of fibre and matrix stiffness's which give the same coupon stiffness for each sample. Each sample has a unique range for the fibre stiffness where Samples 1 and 2 are most similar and Sample 3 requires a higher fibre stiffness. Furthermore, it can be seen that a lower matrix stiffness result in a larger difference in fibre stiffness between the samples. The similarities between the samples converge when increasing the matrix stiffness.

4.4.2 Orthotropy Calibration

The calibration of the orthotropic fibre stiffnesses is performed as described in Section 3.5.2 and the results are presented in Table 4.3 below. From the table, it is observed that there are several parameters that have been calibrated depending on the longitudinal fibre stiffness. In addition to the table, a 2D line plot similar to the result in Section 4.4.1 is presented in Figure 4.14. The figure shows the ranges of the longitudinal fibre stiffness depending on the range of matrix stiffness. It is noted that every curve represents the same sample and its coupon stiffness.

Table 4.3: Calibrated longitudinal fibre stiffness, E_x^f, as well as the parameters depending on the longitudinal fibre stiffness. The resulting coupon stiffness for each sample is also presented.

		Sample 1	Sample 2	Sample 3
E_x^f	[GPa]	21-38	23-42	28-57
$E_y^f = E_z^f$	[GPa]	7-13	8-14	9-19
$G_{xy}^f = G_{xz}^f$	[GPa]	5-9	5-10	7-13
G_{yz}^f	[GPa]	2-3	2-3	2-4
ν_{xy}^f	[-]	0.06	0.06	0.06
$\nu_{xz}^f = \nu_{yz}^f$	[-]	0.35	0.35	0.35
E_m	[GPa]	0.8-2.0	0.8-2.0	0.8-2.0
E_c	[GPa]	1.16	1.79	2.63

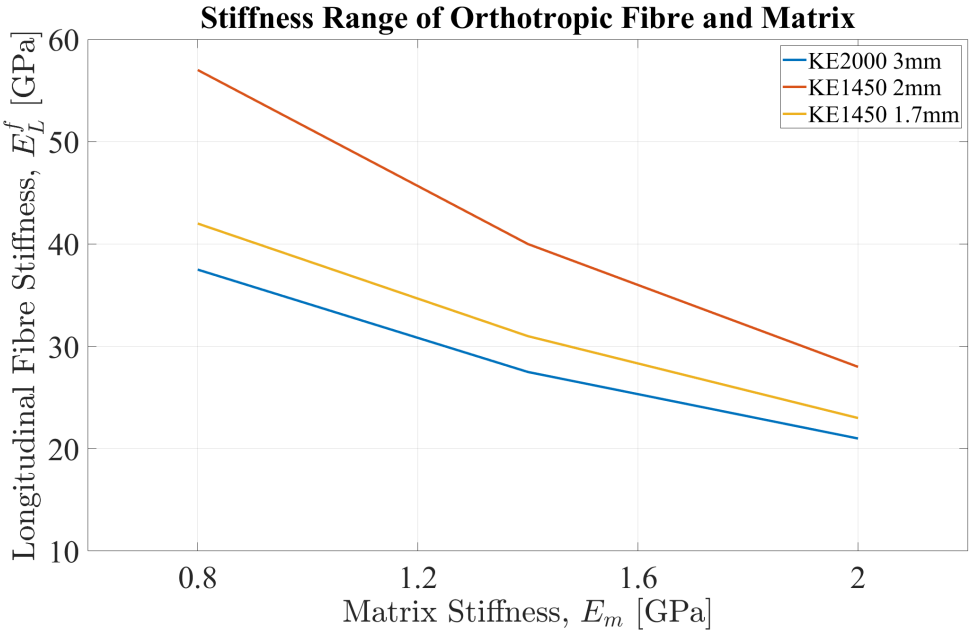

Figure 4.14: Calibrated longitudinal fibre stiffness range as well as the matrix stiffness range. Note that every curve represents one sample and its coupon stiffness.

The result from the elastic orthotropic calibration shows that it is possible to calibrate the material model for all three samples within reasonable constituents stiffness properties. The trend between the samples are similar in Figure 4.14 having orthotropy as in Figure 4.13 for isotropic fibres. This indicates that introducing orthotropy does not have a significant effect in the simulated stress-strain response, in the elastic region. Taking this result into account the continuation of the calibration will be done using isotropic elasticity, as described in Section 4.4.1, to reduce the complexity and number of uncertainties in the constituent properties.

4.4.3 Plasticity Calibration

The plastic calibration has been carried out by varying the scaling parameter of the plastic flow curve. Figure 4.15 illustrates how the simulated stress-strain response is varying when changing the scale factor, σ_{sf}. A lower value of the scale factor corresponds to a lower stress to initiate the plasticity in the matrix elements. This entails a more plastic behaviour for the global stress-strain response.

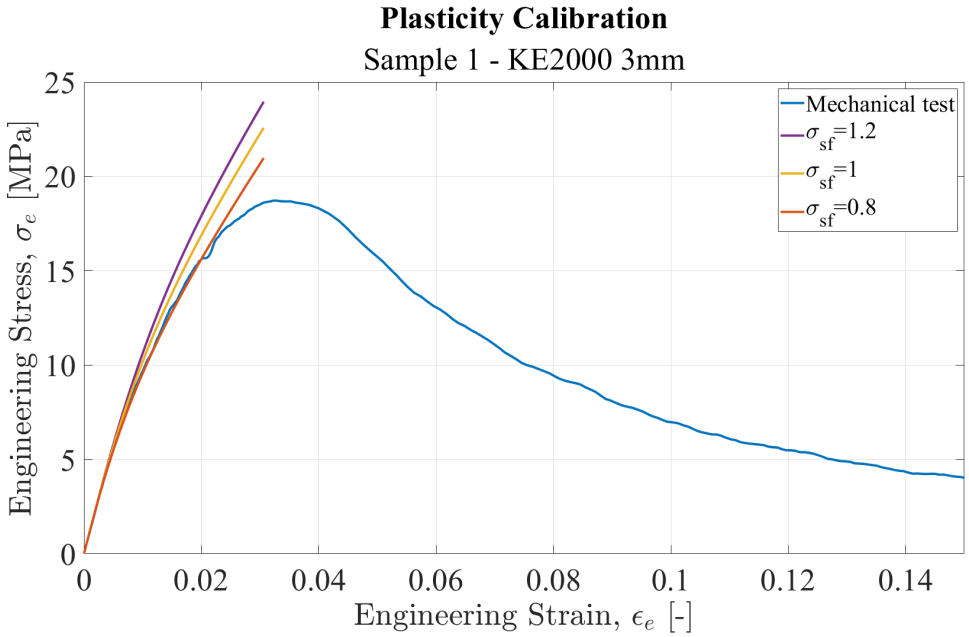

Figure 4.15: Effect in the stress-strain response when varying the scale factor on the plastic flow curve σ_{sf}

Every sample has been calibrated for three stiffness combinations representing the relation between the fibre and matrix stiffness shown in Figure 4.13. In Figures 4.16 - 4.18 one can see the calibrated curves and their corresponding scale factor. When analysing the result one can see that stiffness combination 1 yields the most accurate calibration in all three samples. Combinations 2 and 3 do not match the mechanical test as well when only calibrating the scale factor. The response does not show enough nonlinearity and thereby underestimate the stress-strain response. In the continuation of the material calibration only the first combination will be considered.

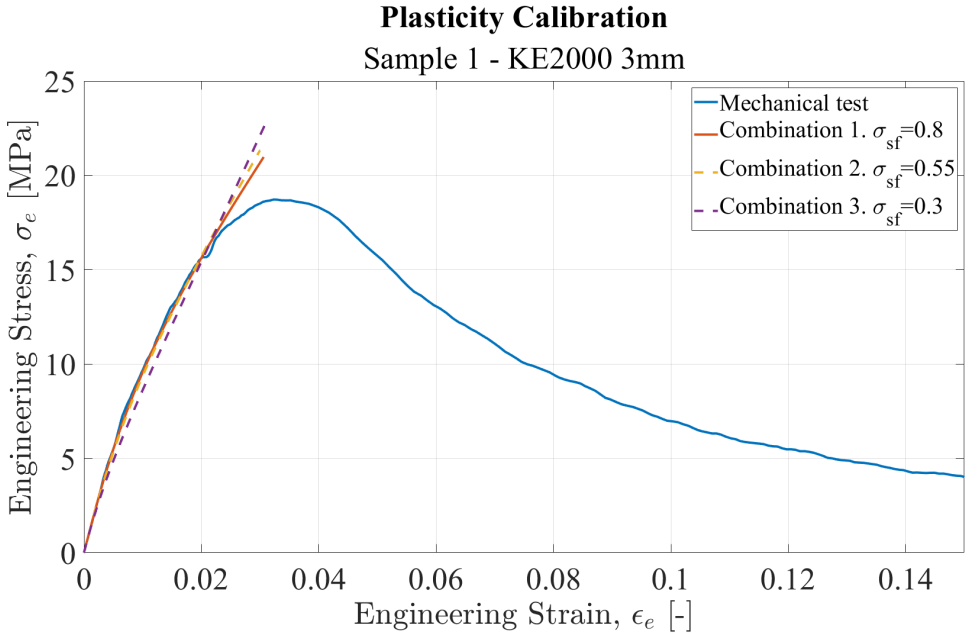

Figure 4.16: Plasticity calibration of Sample 1 and its three stiffness combinations. σ_{sf} represent the scale factor on the plastic flow curve.

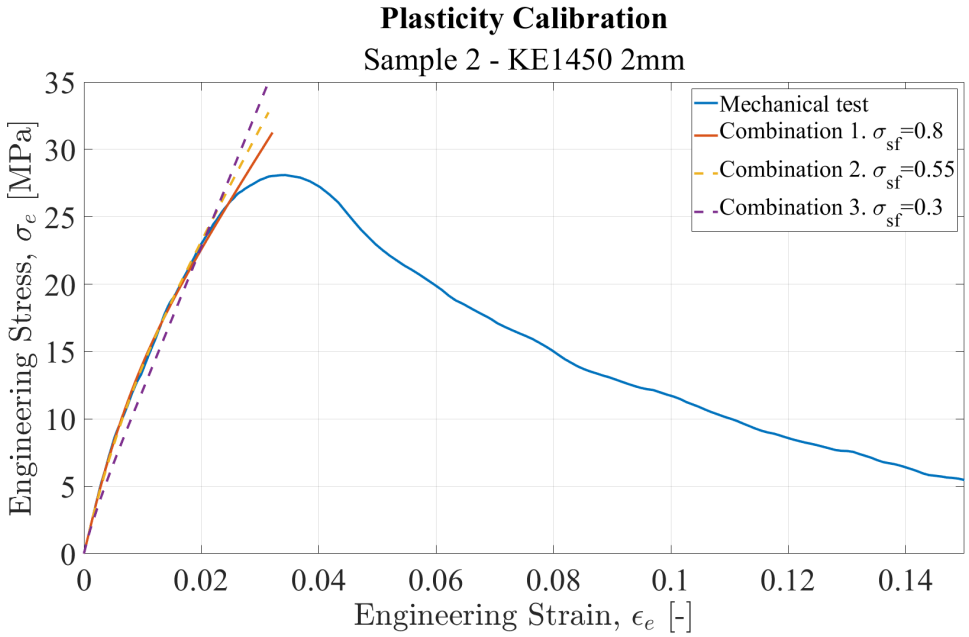

Figure 4.17: Plasticity calibration of Sample 2 and its three stiffness combinations. σ_{sf} represent the scale factor on the plastic flow curve.

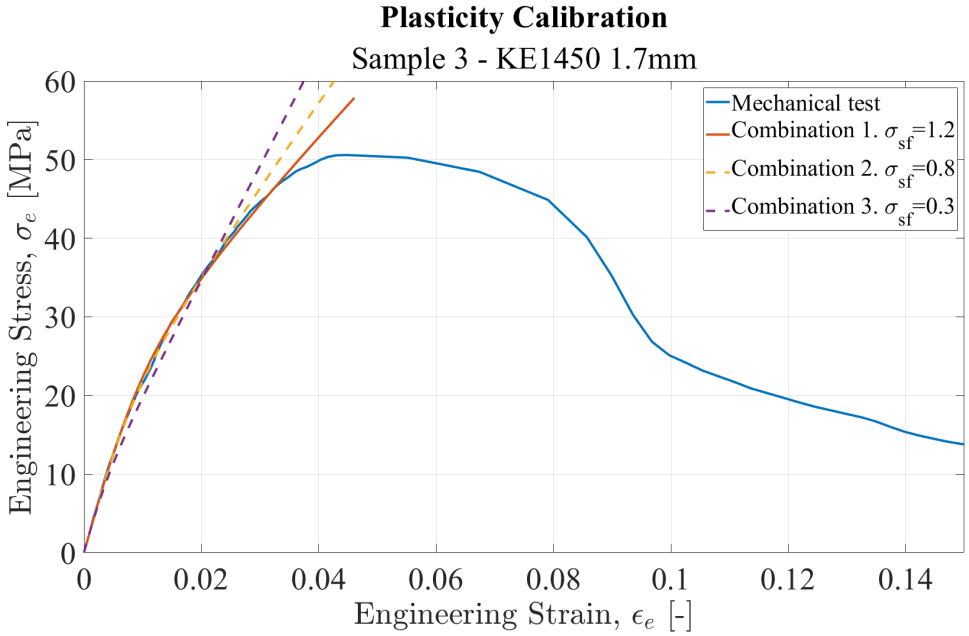

Figure 4.18: Plasticity calibration of Sample 3 and its three stiffness combinations. σ_{sf} represent the scale factor on the plastic flow curve.

In Table 4.4 each calibrated scale factor for the combinations is presented together with its stiffness parameters. From this, it is also clear that a higher matrix stiffness yields a scaling factor closer to 1. This indicates that a higher matrix stiffness results in more non-linearity and thereby capturing the response from the mechanical test to a greater extent. It is also noted that Samples 1 and 2 have identical scale factor values no matter the stiffness combination. Furthermore, Sample 3 requires a higher scale factor value to capture the mechanical response.

Table 4.4: Calibrated fibre and matrix stiffness together with the scale factor of the flow curve, σ_{sf}.

Sample 1	E_f [GPa]	E_m [GPa]	σ_{sf} [-]
Combination 1	10	2.0	0.80
Combination 2	12.5	1.4	0.55
Combination 3	17	0.8	0.3
Sample 2	E_f [GPa]	E_m [GPa]	σ_{sf} [-]
Combination 1	11	2.0	0.80
Combination 2	14	1.4	0.55
Combination 3	20	0.8	0.3
Sample 3	E_f [GPa]	E_m [GPa]	σ_{sf} [-]
Combination 1	12	2.0	1.2
Combination 2	17	1.4	0.80
Combination 3	25	0.8	0.3

4.4.4 Damage Calibration

The damage calibration has been carried out by varying the strain to failure of the fibre elements. Figure 4.19 illustrates how the simulated stress-strain response is varying when changing the strain to failure, ε_{fU}. From the figure one can tell that the peak stress is directly dependent on the strain to failure value. A lower strain value corresponds to a lower peak stress and the other way around.

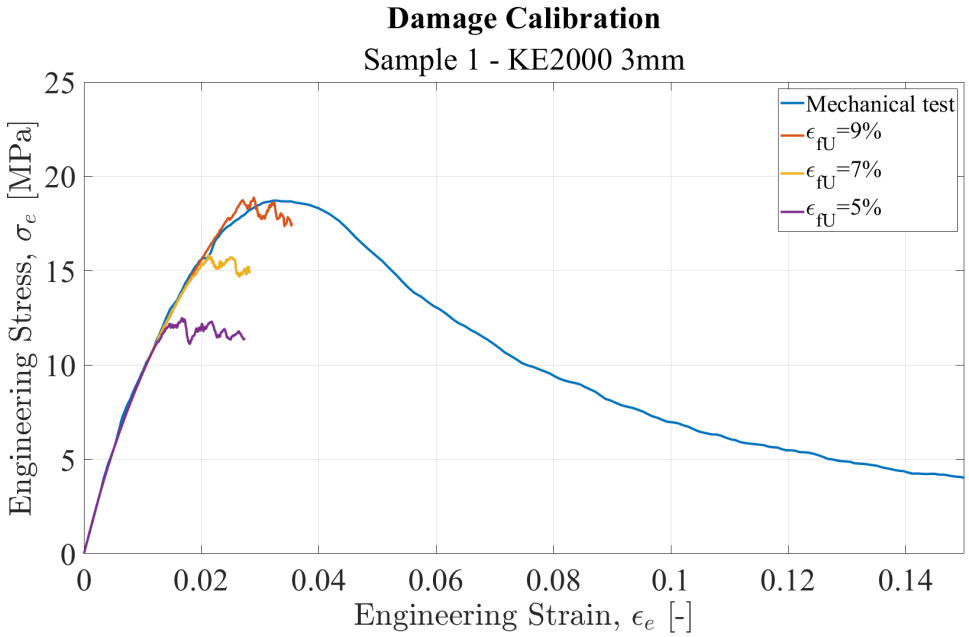

Figure 4.19: Effect in the stress-strain response when varying ultimate fibre strain ε_{fU}

The result from the damage calibration and the stress-strain response is found in Figures 4.20 - 4.22. The calibration successfully captures the peak stress in all three samples. The final calibration of the mechanical properties can be found in Table 4.5. All the samples show similar calibrated properties in the elastic region. Furthermore, Sample 1 and 2 has identical properties in both the plastic and damage calibration. Sample 3 requires a higher value in the fibre failure strain in order to capture the behaviour.

Table 4.5: Calibrated mechanical properties for all three samples. E_f is the fibre stiffness, E_m is the matrix stiffness, σ_{sf} is the plasticity scaling factor and ε_{fU} is the ultimate fibre strain.

	E_f [GPa]	E_m [GPa]	σ_{sf} [-]	ε_{fU} [-]
Sample 1	10	2.0	0.8	0.09
Sample 2	11	2.0	0.8	0.09
Sample 3	12	2.0	1.2	0.13

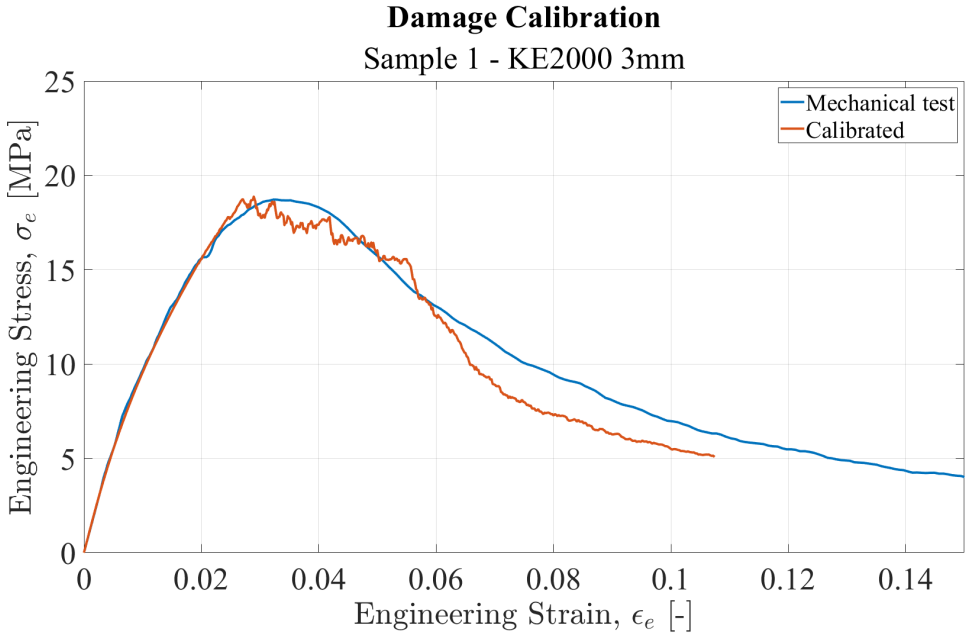

Figure 4.20: Calibrated stress-strain curve for Sample 1, ε_{fU}=9%

Furthermore, the predictability between the different samples is investigated. This is achieved by applying the calibrated mechanical properties from Sample 1 to Samples 2 and 3, and observing how well the predicted stress-strain responses aligned. The results of the predictability are represented by the yellow curves in Figures 4.21 and 4.22. The prediction of the stress-strain response in Sample 2 is nearly a perfect match. However, there are slight differences in the initial stiffness, leading to disparities in plasticity and peak stress. The curve from the prediction of Sample 3 does not match as well. Although the initial stiffness is close, both the plasticity and damage region show deviations. However, the general trend for Sample 3 is captured by the prediction.

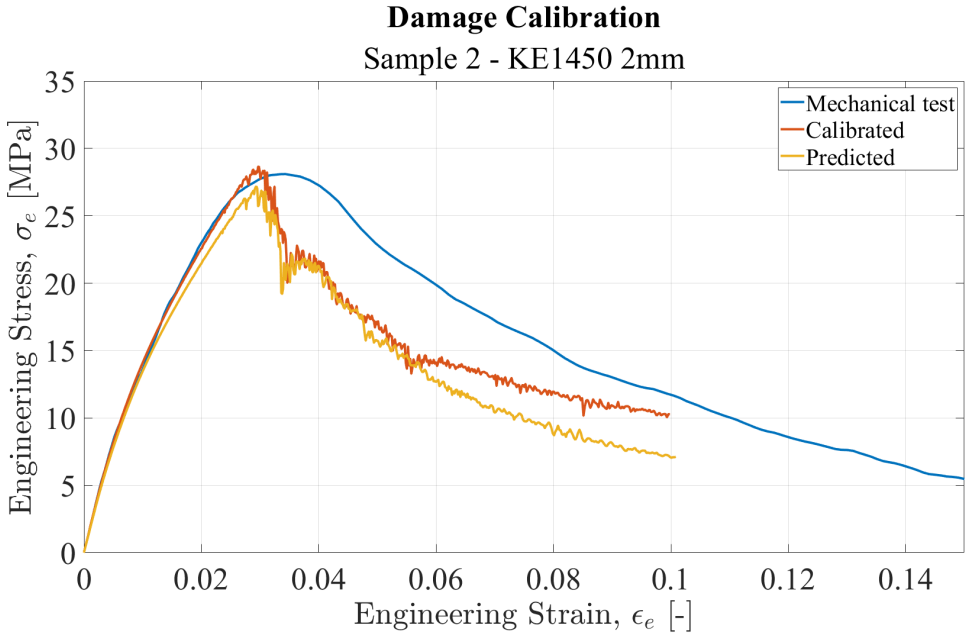

Figure 4.21: Calibrated stress-strain curve for Sample 2 together with the predicted response, calibrated failure strain ε_{fU}=9%

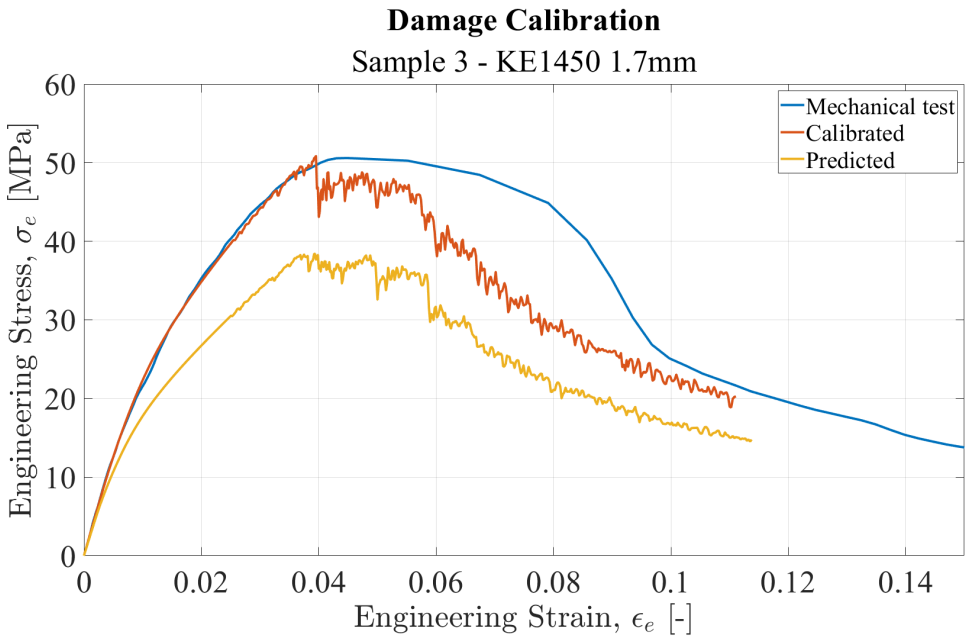

Figure 4.22: Calibrated stress-strain curve for Sample 3 together with the predicted response, calibrated failure strain ε_{fU}=13%

In addition to calibrating the peak stress using the fibre failure strain, the damage calibration also yields interesting results in the behaviour after the peak. In Sample 1 (Figure 4.20), the simulated response is able to accurately capture the trend after the peak. Sample 2 (Figure 4.21) exhibits a brittle failure in the simulation, whereas the mechanical test shows a more ductile behaviour. In Sample 3 (Figure 4.22), the trend is similar between

the simulation and the mechanical test. The simulation exhibits ductile behaviour similar to the mechanical test, which is not present in either of the other samples. Furthermore, the simulated failure modes can be found in Section 4.4.5, where the differences and similarities are presented both between the samples and in comparison to the mechanical test.

4.4.5 Failure Modes

In the following section all the failure modes from the simulation are presented together with a comparison to the physical failure mode. For every sample the failure mode is illustrated by two figures, one in a 3D-view and the other from above. The result from Sample 1 is presented in Figure 4.23 and shows a failure mode localised at the thinnest region of the coupon. The crack is propagating straight from edge to edge. Comparing this to the the failure mode from the mechanical test one can see similarities in both the position of the failure and the crack surface. Based on this observation it is concluded that the failure mode have been captured in the simulation.

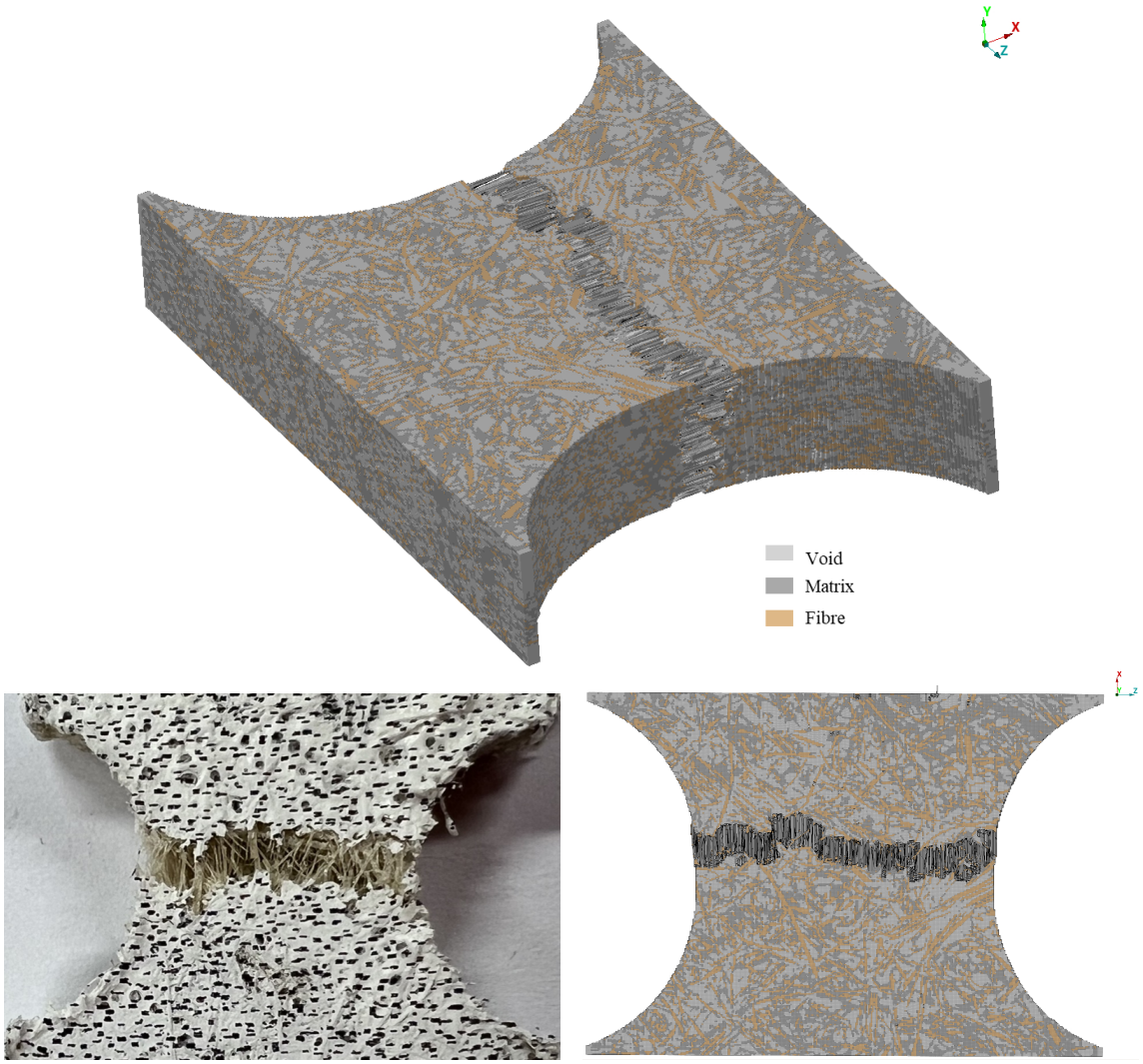

Figure 4.23: Failure mode from the simulation and mechanical test of Sample 1

The result of Sample 2 is presented in Figure 4.24 where one can see that the crack propagates from both sides. Both of the cracks are initiated at the thinnest part of the coupon and propagate inwards. However, the cracks do not connect. Instead two separate cracks are formed which is different in comparison to the failure mode in the mechanical test. In the mechanical test the failure mode is similar to the first sample, which is localised in the middle as one single crack.

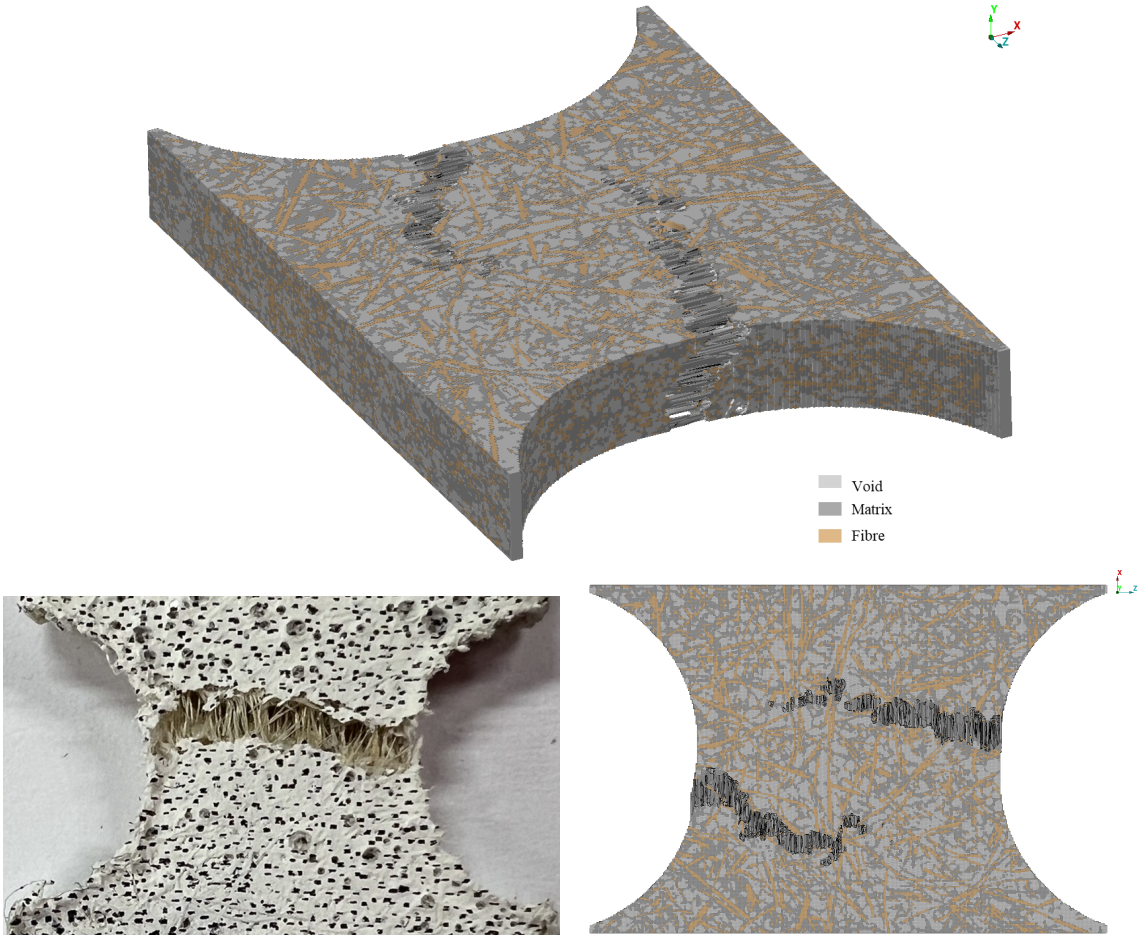

Figure 4.24: Failure mode from the simulation and mechanical test of Sample 2

The result of Sample 3 is presented in Figure 4.25 where one can see that the crack propagates from the edge inwards but slightly closer to the edge. Looking at the failure mode from the mechanical test this is also different as the crack is propagating with an angle. The simulated and mechanical failure mode does not match fully but both show a different behaviour in comparison to the other two samples. One can say that the simulation captures a similar behaviour but does not match the mechanical failure mode fully.

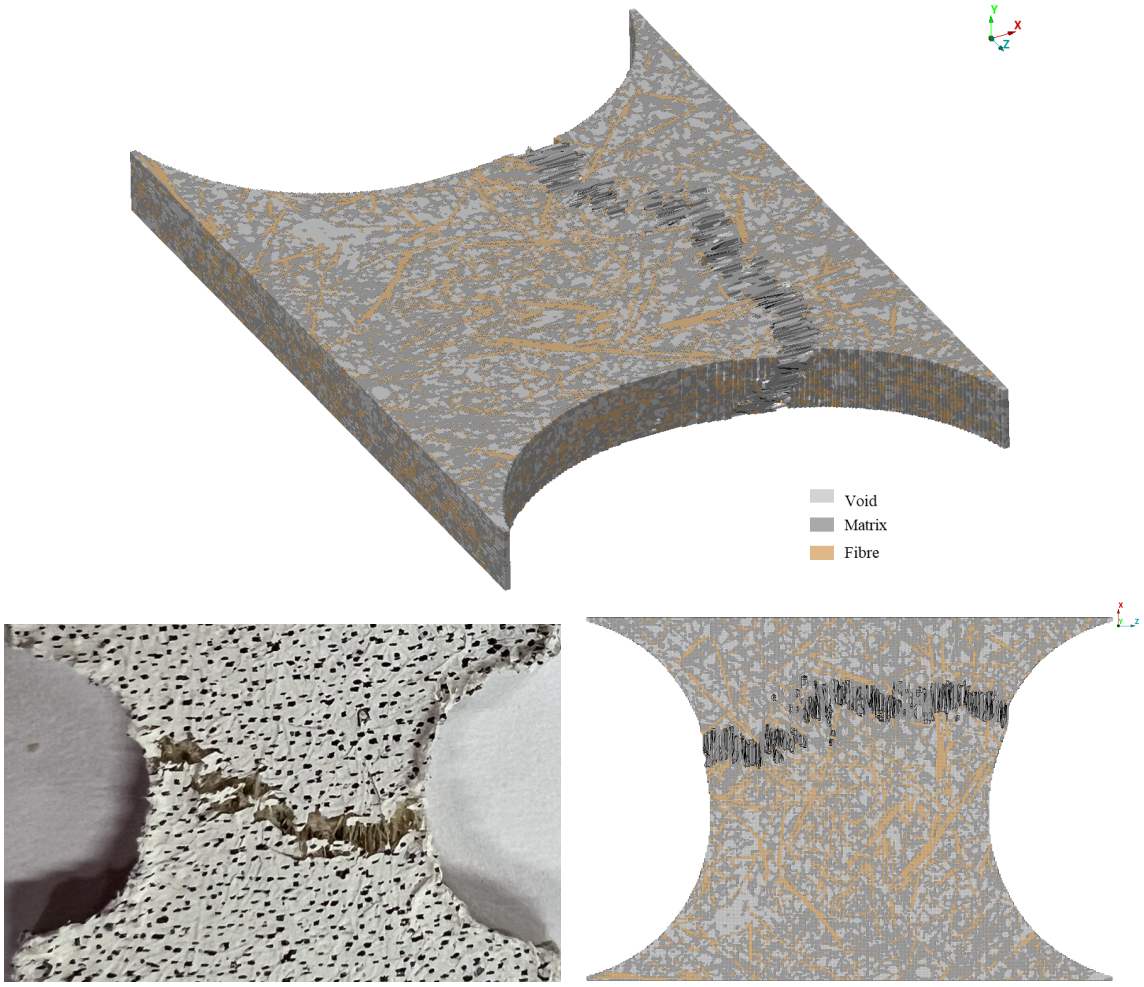

Figure 4.25: Failure mode from the simulation and mechanical test of Sample 3

5
Discussion

5.1 X-ray computer tomography aided engineering

The results from the XAE process are presented in Section 4.1 and from these results a number of interesting observations has been obtained. In Figures 4.1, B.1 and B.6 the reconstructed images from the image acquisition are presented. In imaging there are usually two conflicting goals; high resolution and large field of view. The chosen resolution allowed to scan the full notched area and for an accurate segmentation of voids, matrix and fibres later on in the process. It should also be mentioned that the intensity issue described earlier is not visible in these figures which should entail that the grey-scale analysis will yield good results. When considering the segmentation images in Figures 4.3, B.3 and B.8 it is observed that the microstructure is correctly captured which is also confirmed by the comparison of the analytical and the FE simulation volume fractions of void, matrix and fibre.

Given the complex microstructure with randomly oriented fibres and large void contents as well as the limited contrast in the image data between fibres and matrix a segmentation algorithm solely basing on histograms and thresholds cannot reflect the complexity of the task. Due to this, the introduction of the commercial software RETOMO is crucial for the accuracy of the results. The challenge with the histogram analysis is that from the obtained histograms presented in Figures 4.2, B.2 and B.7 has only two clear peaks. Remember that we are interested in the consideration of three different phases void, matrix and fibres. This means that some values are overlapping leading to issues when determining the exact thresholds, see leftmost schematic in Figure 5.1. To overcome this issue, this procedure is done in an iterative fashion where the FE mesh volume fractions are compared to the analytical volume fractions until a satisfying match is obtained. In the figure, it is observed that the chosen threshold values are indicated by the two vertical grey lines. The rightmost image in Figure 5.1 shows the histogram for Sample 1 and its corresponding threshold values presented as the two vertical lines. When looking at this image it is noted that the segmentation process is difficult as we experience a lot of overlapping of the different parts void, matrix and fibre, especially for matrix and fibre. This overlapping yields that some fibre parts will be detected as matrix and vice versa, which is a problem with the overall segmentation process. However, as the segmentation is done through an iterative process where the volume fractions are compared to the analytical then a satisfying segmentation result can be obtained. This approach however requires accurate analytical volume fraction numbers.

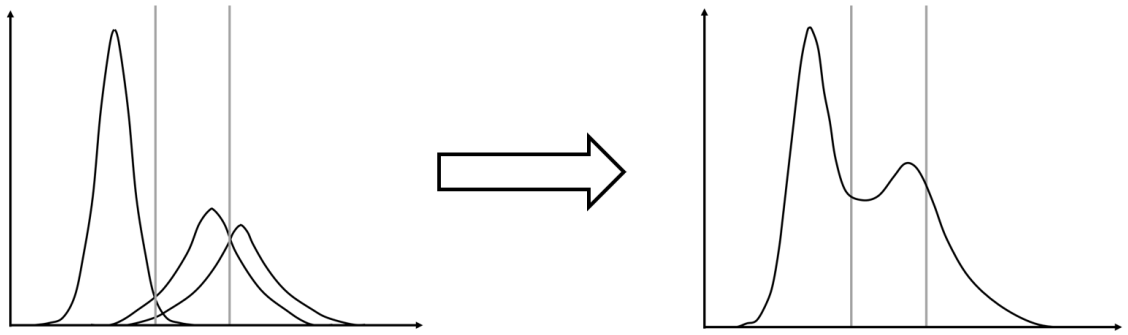

Figure 5.1: Histogram of the grey-scale image data from the image acquisition for all samples.

Further in the analysis of the different samples, an interesting observation is when comparing the shape of the histograms. In Figure 5.2, histograms from all three samples are presented. Both the x- and the y-axis are normalised to make the comparison clearer. The grey-scale values on the x-axis are defined from 0 to 1 whereas the y-axis presents a normalised pixel value against the sum of all pixel for each image. It is noted that Sample 1 and 2 have similar behaviour and the curves are more or less on top of each other. When considering the characteristics for Sample 3 it is observed that the rightmost peak is higher than the leftmost peak, compared to Samples 1 and 2 where it is the other way around. This means that Sample 3 has more fibre and matrix material meaning that there are less voids. This observation is also observed from both the grey-scale images in Figures 4.1, B.1 and B.6 and from the segmentation images in Figures 4.3, B.3 and B.8.

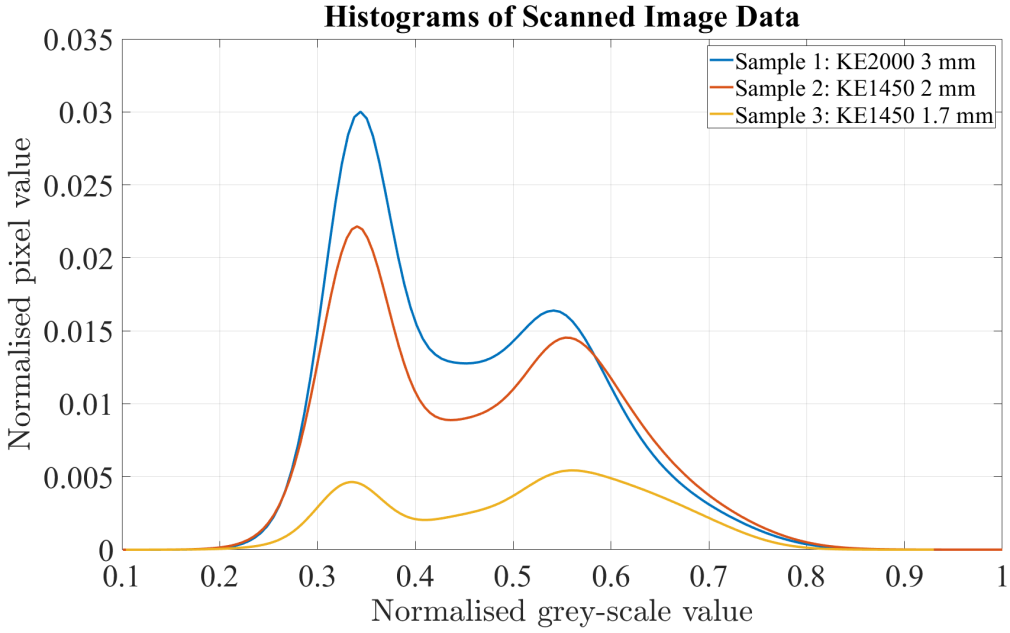

Figure 5.2: Histogram of the grey-scale image data from the image acquisition for all samples.

5.2 Mechanical tests and microscopy

The mechanical test results presented in Section 4.2 show the stress-strain responses and the failure modes from the tests of the samples. From these results it is observed that both the responses and the failure modes for Sample 1 and 2 are more or less similar. Even though the materials have a different areal weight, they have similar densities. From this it is noted that the density of the material has an impact on the material behaviour. When comparing the response trend between the samples it is noted that Sample 3 has more of a ductile behaviour compared to Samples 1 and 2. This means that as the composite mat is pressed more, the density is higher and the material is characterised by a different material behaviour. The amount of applied pressure in manufacturing has a major impact on the response of the material.

Moving on to the analysis done with the microscope, it is observed that as the material is pressed more, the matrix is more and more smeared out. This affects the material behaviour as the matrix represents a larger portion of the sample as there are much less voids as the sample is compressed more. Furthermore, it was also observed from the microscopy analysis that the fibres in the fracture surface show signs of brittle tensile failure of the fibres. This is concluded from the straight edges of which the fibres are fractured, it is also possible to see a lip at the end of the fibres which also is an indication of a tensile failure.

When combining the findings from both the mechanical tests and the microscopy analysis it is noted that the difference between Sample 1 and 2 and Sample 3 is even clearer. We have two samples with similar density which show similar behaviour, both in the stress-strain response and when considering the failure mode of the fracture. This means that it is possible to change the response of the material, to more of a ductile or brittle behaviour, by changing the density of the composite.

5.3 FE simulations

From the elasticity calibration results, presented in Section 4.4.1, it is observed that a range of possible solutions is presented. This range occurs due to the uncertainty of the constituents material properties, as described in Section 3.5.1. If the constituent properties were known, it would still be beneficial to introduce a range due to the unknown fibre-matrix bonding. The presented calibrated stiffness of fibre and matrix should not be considered as a unique solution as there are multiple combinations of constituents stiffnesses that yield the same coupon stiffness. We have only considered the stiffness of the sample on a macro level while calibrating constituents on the micro level.

The orthotropy results, presented in Section 4.4.2, show that it is possible to use orthotropic fibres in the model. From this it is noted that there are several similarities with the results from the isotropic elasticity analysis. Additionally, the orthotropy analysis deals with far more variables, and are a heavier model, led to exclusion from the continuation of the project. The similarities in the results are due to the geometrical directions of the

fibre elements in the mesh. This means that the fibre orientations themselves do not have a huge influence on the already complex model.

From the plasticity results, presented in Section 4.4.3, it is observed that to fully capture the nonlinearity of the material behaviour a higher matrix stiffness is needed. This means either the actual matrix stiffness is in the high region of the presented span or there are some physics that are not captured by only scaling the plasticity flow curve. For instance this could be damage degradation of the matrix prior to the peak load. These two explanations are not elaborated in this thesis but remain for future work on the model.

The final result of the simulations are shown in Table 4.5 where the calibrated parameters from elasticity, plasticity and damage are presented. From this table, it is noted that Samples 1 and 2 are more or less the same whereas Sample 3 differs both in the plasticity and damage parameters. The difference between these samples are density and from the microscopy analysis presented in Section 4.3 it was observed that the matrix was more smeared out for Sample 3 compared to Samples 1 and 2. With this, Sample 3 has more matrix and less voids per volume which means higher density. It seems that there is a correlation for the scale factor of the plasticity flow curve and the strain to failure to the density of the sample. We see that a higher density yields a higher strain to failure for the fibre as well as a higher scale factor of the plasticity flow curve.

In Figures 4.20 - 4.22 the stress-strain responses from the damage analysis are presented. To model this, a brittle tensile fibre failure is introduced as explained in Section 3.5.4. This approach captures the peak stress accurately and to some extent the behaviour after the peak stress. With this approach other physical phenomena are indirectly captured due to the similarities between the simulations and the mechanical tests. In the physical coupon more damage types such as matrix failure, fibre pull-out or shear failure might also occur. If one would want the exact failure mode of the samples it could be interesting to investigate this further.

5.4 General discussion

The process of going from a CT scanned image to a mesh for FE analysis is presented in Figure 5.3 below. From the figure it is observed that the resolution form the scan is fine enough to capture continuous fibres. Further, it is noted that the phase segmentation, top right image, manages to characterise the fibres as fibres, matrix surrounding the fibres as matrix and the voids inside the material as voids. In the bottom left image the mesh is presented where it is observed that the microstructure is very similar to the scanned image on the top left part of the figure. This even though the mesh has been sub-sampled with a sub-sampling rate of 5. In the bottom right an image of the damaged sample is presented. From this it is noted that the microstructure is captured and characterised throughout all stages in the analysis. From this it is concluded that X-ray computer tomography aided engineering is a good methodology when complex microstructures should be analysed. With this being said, it should also be mentioned that the methodology also could be used for other materials with simpler microstructures as well. One big advantage in those cases

are that the segmentation procedure should be a far more smooth process with less error sources.

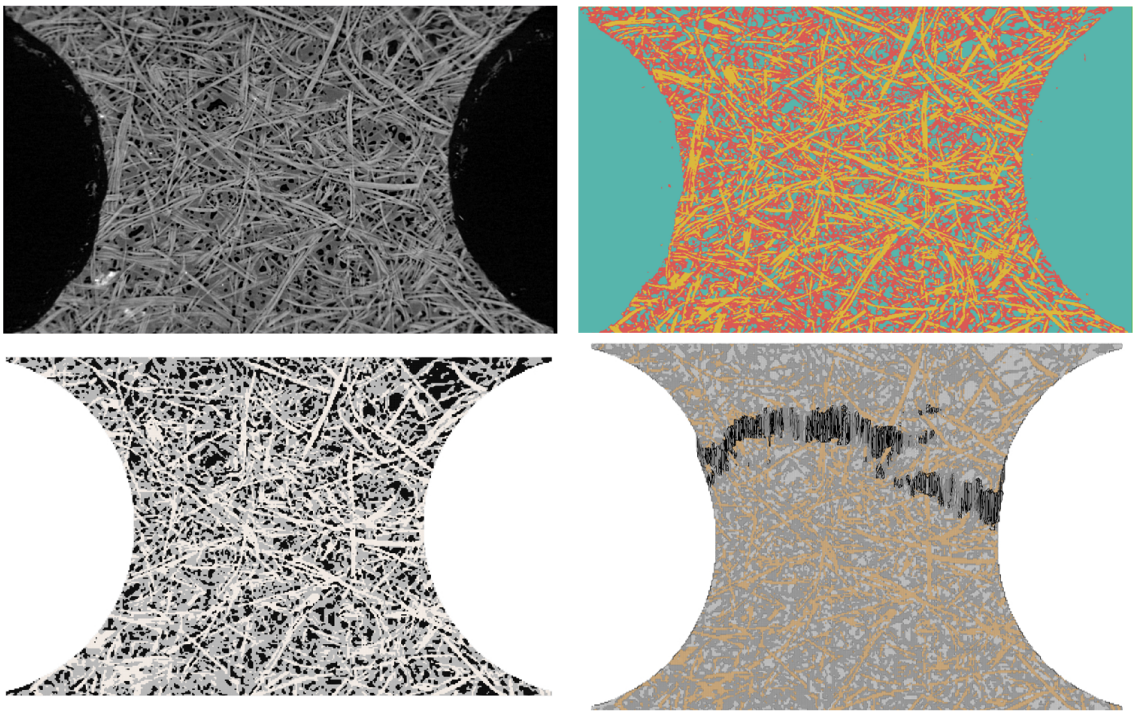

Figure 5.3: Images from the entire XAE to simulation of damage process. The microstructure in the images is an example and are Sample 3.

6
Conclusions

Characterising a natural fibre composite on the coupon level using the XAE methodology has not been done until this day. In this thesis a methodology of such an analysis is presented. The objective of this thesis work was to determine if the XAE process is applicable for natural fibre composites and if so, to find if it is possible to correlate a virtual coupon test to a mechanical test. From the presented results and discussions it is clear that the XAE process is applicable for natural fibre composites and further it was found that correlation of a virtual test coupon is possible. To do so the constituents elasticity, plasticity and damage parameters are calibrated successfully. During the thesis work, it was also found that predicting material behaviour is possible for samples with similar densities.

6.1 Future Work

To ensure that virtual testing of materials can be even further developed it is important to investigate the possibility of predicting the material behaviour even further. As mentioned in this report it is possible to properly predict the material behaviour for material samples of similar densities. It remains for future work to validate the model for a broader range of densities.

An interesting topic to further investigate is how the material is affected by how much it is pressed in manufacturing. Remember that the thickness difference for Sample 2 and 3 in this report is only 0.3 mm but the two samples behave totally differently. An investigation on whether the matrix and/or fibre are affected by the pressing would be of interest.

In the final stages of the calibration, the damage calibration, it is mentioned that the focus lies on capturing the peak load. Less attention has been paid to accurately model the behaviour after the peak load. To develop the model even further, the effect of damping and a viscous behaviour is of interest. By introducing this it should be possible to get rid of some of the oscillations and get an even better fit after the peak load.

One final note that could be interesting to examine is how this XAE procedure is applicable for other materials. This thesis has proven that complex microstructure which is hard to distinguish and irregular porosity can be analysed by this method. It is believed that this method can be easily transferred to metal alloys where only the grain structure and possible voids are of interest.

Bibliography

[1] N. Saba, M. T. Paridah and M. Jawaid, "Mechanical properties of kenaf fibre reinforced polymer composite: A review," *Construction and Building Materials*, vol. 76, pp. 87–96, Feb. 2015.

[2] Robert M. Auenhammer, Lars P. Mikkelsen, Leif E. Asp and Brina J. Blinzler, "Automated X-ray computer tomography segmentation method for finite element analysis of non-crimp fabric reinforced composites," *Composite Structures*, vol. 256, 2021.

[3] Tuukka Verho, Stefania Fortino, Petr Hradil *et al.*, "Biocomposite modeling by tomographic feature extraction and synthetic microstructure reconstruction," *Composites Science and Technology*, vol. 230, p. 109 713, Nov. 2022.

[4] Alp Karakoç, Arttu Miettinen, Jussi Virkajrvi and Roberts Joffe, "Effective elastic properties of biocomposites using 3D computational homogenization and X-ray microcomputed tomography," *Composite Structures*, vol. 273, p. 114 302, Oct. 2021.

[5] Ayou Hao, Haifeng Zhao and Jonathan Y. Chen, "Kenaf/polypropylene nonwoven composites: The influence of manufacturing conditions on mechanical, thermal, and acoustical performance," *Composites Part B: Engineering*, vol. 54, no. 1, pp. 44–51, Nov. 2013.

[6] Stefan Hesseler, Scott E. Stapleton, Lars Appel, Sven Schöfer and Boris Manin, "Modeling of reinforcement fibers and textiles," *Advances in Modeling and Simulation in Textile Engineering: New Concepts, Methods, and Applications*, pp. 267–299, Jan. 2021.

[7] Bhagwan D Agarwal, Lawrence J Broutman and K Chandrashekhara, *Analysis and Performance of Fiber Composites*. Newark, UNITED STATES: John Wiley & Sons, Incorporated, 2017.

[8] Reza Mahjoub, Jamaludin Mohamad Yatim, Abdul Rahman Mohd Sam and Sayed Hamid Hashemi, "Tensile properties of kenaf fiber due to various conditions of chemical fiber surface modifications," *Construction and Building Materials*, vol. 55, pp. 103–113, Mar. 2014.

[9] O. M.L. Asumani, R. G. Reid and R. Paskaramoorthy, "The effects of alkali–silane treatment on the tensile and flexural properties of short fibre non-woven kenaf reinforced polypropylene composites," *Composites Part A: Applied Science and Manufacturing*, vol. 43, no. 9, pp. 1431–1440, Sep. 2012.

[10] R Clack, "Towards a complete description of three-dimensional filtered backprojection," *Physics in Medicine & Biology*, vol. 37, no. 3, 1992.

[11] Britta Weber, Garrett Greenan, Steffen Prohaska *et al.*, "Automated tracing of microtubules in electron tomograms of plastic embedded samples of Caenorhabditis

elegans embryos," *Journal of Structural Biology*, vol. 178, no. 2, pp. 129–138, May 2012.

[12] Ewa Pietka, "Image Standardization in PACS," in *Handbook of Medical Imaging*, Academic Press, Jan. 2000, pp. 783–801.

[13] André Marion, *Introduction to Image Processing*. Springer US, 1991.

[14] John Holmes, Silvano Sommacal, Raj Das, Zbigniew Stachurski and Paul Compston, "Digital image and volume correlation for deformation and damage characterisation of fibre-reinforced composites: A review," *Composite Structures*, vol. 315, p. 116 994, Jul. 2023.

[15] Karan Shah, Subramani Sockalingam, Hannah O'Brien *et al.*, "Sub-microscale speckle pattern creation on single carbon fibers for scanning electron microscope-digital image correlation (SEM-DIC) experiments," *Composites Part A: Applied Science and Manufacturing*, vol. 165, p. 107 331, Feb. 2023.

[16] Mahoor Mehdikhani, Mohammadali Aravand, Baris Sabuncuoglu, Michaël G. Callens, Stepan V. Lomov and Larissa Gorbatikh, "Full-field strain measurements at the micro-scale in fiber-reinforced composites using digital image correlation," *Composite Structures*, vol. 140, pp. 192–201, Apr. 2016.

[17] Prakash Jadhav, Gruhalakshmi Yella and Anitha Azmeera, "Ply level strain measurement in composites using digital image correlation," *Materials Today: Proceedings*, Mar. 2023.

[18] John O Hallquist, *LS-DYNA ® THEORY MANUAL*, 2006.

[19] Kenneth Runesson and Ragnar Larsson, *The Primer - Constitutive modeling of engineering materials theory and computation*. Chalmers University of Technology, 2021.

[20] Karl Schweizerhof and Wilhelm J H Rust, "Quasi-Static Analyses Using Explicit Time Integration-Applications of LS-DYNA," 1999.

[21] Ted Belytschko, Wing Kam Liu, Brian Moran and Khalil Elkhodary, *Nonlinear Finite Elements for Continua and Structures*, 2nd ed. New Jersey: John Wiley & Sons, Incorporated, Dec. 2014.

[22] N. Jeppesen, V. A. Dahl, A. N. Christensen, A. B. Dahl and L. P. Mikkelsen, "Characterization of the fiber orientations in non-crimp glass fiber reinforced composites using structure tensor," in *IOP Conference Series: Materials Science and Engineering*, vol. 942, IOP Publishing Ltd, Oct. 2020.

[23] ASTM, *D2734-16, Standard Test Methods for Void Content of Reinforced Plastics*, 2016.

[24] H.A. McKenna, J.W.S. Hearle and N. O'Hear, "Ropemaking materials," in *Handbook of Fibre Rope Technology*, Woodhead Publishing, Jan. 2004, pp. 35–74.

A

Parameter study

Throughout this project, a number of assumptions and parameters have been set based on the authors judgement. To make sure that these assumptions do not affect the results in a way that would change the outcome some parameter studies are made. Two parameters that were set during the XAE process are the sub-sampling rate of the "Voxels to hexas" function as well as the angular search increment during the fibre tracking procedure. In addition to this, a parameter study on how the Poisson's ratio affects the coupon stiffness in the elastic case is presented.

A.1 Effect of mesh size

In order to study how the mesh procedure in RETOMO "Voxels to hexas" affects the coupon stiffness a parameter study on the sub-sampling rate has been made. As explained in Section 3.2.4 a sub-sampling rate of 5 has been used in the presented results earlier in the report. In addition to this other sub-sampling rates has been used to compute the coupon stiffness. The sub-sampling rates considered in this study is 3, 5, 7 and 9. In Table A.1 the normalised stiffness, the number of elements and simulation times are presented.

Table A.1: Parameter study on mesh size where the sub-sampling rate, a normalised stiffness, the number of elements and the simulation time is presented. 480 cores are used for each simulation.

Sub-sampling rate	Normalised stiffness	Number of elements	Simulation time
3	1.01	14,935,145	02:36:15
5	1	3,235,412	00:22:01
7	1.01	1,191,652	00:07:18
9	1.11	550,706	00:02:45

In addition to studying the normalised coupon stiffness for the different mesh sizes it is also interesting to consider how the micro structure is affected by the sub-sampling rate. In Figures A.1 - A.4 the micro structures of the four different meshes are presented.

Figure A.1: The mesh generated from "Voxels to hexas" function in the commercial software RETOMO. With a sub-sample rate of 3, the number of elements is 14,935,145.

Figure A.2: The mesh generated from "Voxels to hexas" function in the commercial software RETOMO. With a sub-sampling rate of 5, the number of elements is 3,235,412.

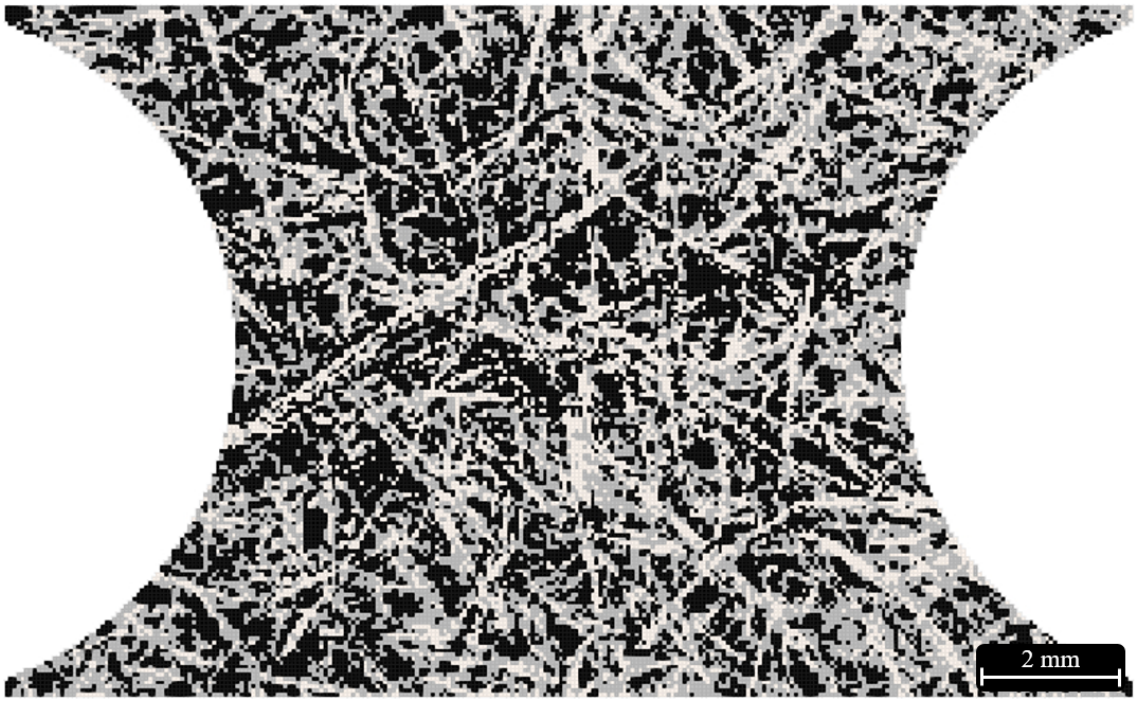

Figure A.3: The mesh generated from "Voxels to hexas" function in the commercial software RETOMO. With a sub-sample rate of 7, the number of elements is 1,191,652.

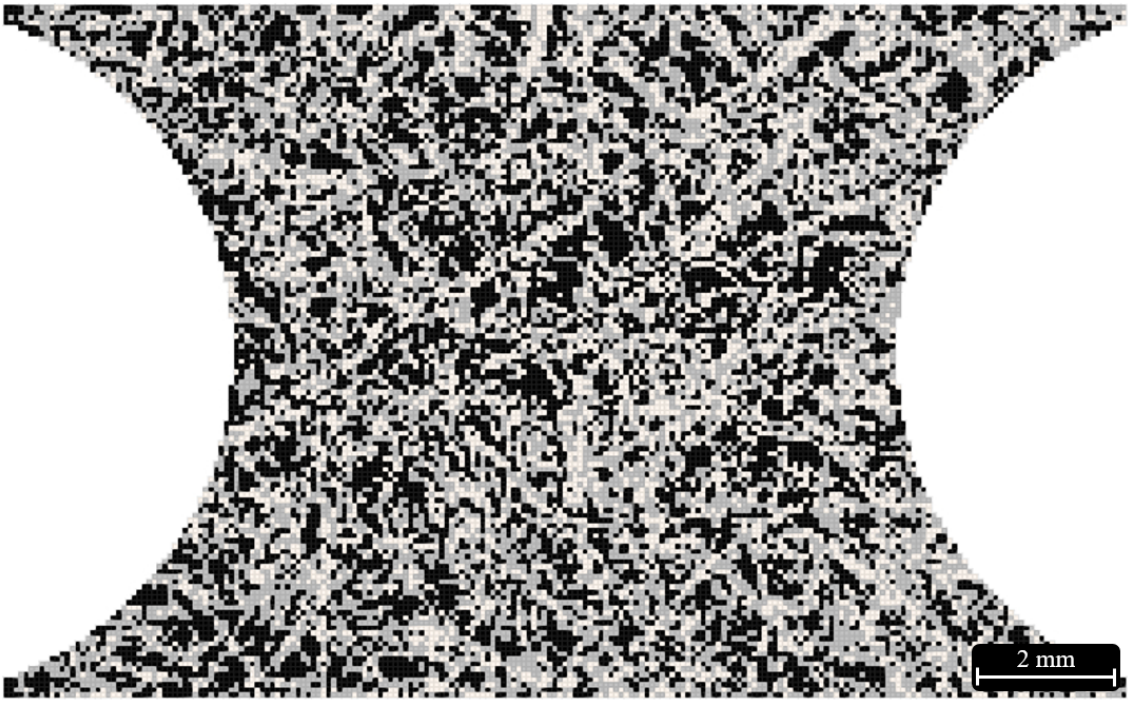

Figure A.4: The mesh generated from "Voxels to hexas" function in the commercial software RETOMO. With a sub-sample rate of 9, the number of elements is 550,706.

From Table A.1 it is observed that the effect on the elastic stiffness of the coupon is limited for different mesh sizes. With this in mind, it is interesting to observe the number

of elements and the simulation times presented in the table. From this information it is clear that the most refined mesh is way to heavy to run. Remember that the presented simulation times are for a fully isotropic elastic model. This means as the more complex material definitions will be added, the simulation time will increase drastically. With this being said it is unfeasible to go for sub-sampling rate 3. Another interesting observation that is done in this analysis is regarding the microstructures presented in Figures A.1 - A.4. From these images it is observed that sub-sampling rates 7 and 9, Figures A.3 and A.4, could be ruled out as the mesh is too coarse to properly capture the continuous fibres in a good way.

To summarise this parameter study it is noted that the number of elements, the simulation time and the microstructure plays an important role. The resulting sub-sampling rate that has been used throughout the project is a sub-sampling rate of 5.

A.2 Effect of the angular search increment

The angular search increment is a measure of the angle which RETOMO uses to determine the fibre direction. The procedure is such that for every pixel in the image, a guess on the fibre direction is made. With a angular search increment of 45 degrees, the guesses will occur 45 degrees apart. For each guess a correlation value is calculated, as described in Section 3.2.3, meaning that if an angular search increment of 45 degrees is used then 8 angles are investigated. Changing the value to e.g. 10 degrees then makes for 36 different angles being checked for each pixel. This is a very time consuming procedure but to capture the right fibre orientations it is crucial to use a fine angular search increment.

A parameter study showing how the angular search increment affects the results is presented in Table A.2 below. The elastic analysis considers orthotropic fibres and an isotropic matrix. From the table, it is observed that the angular search increments 45, 30, 15 and 10 have been studied. Further, it is noted that the effect on the normalised stiffness is limited for different angular search increments. When considering the number of fibres it is a big spread in how many fibres are detected by the fibre tracking. From the table, it is observed that the amount of fibre has a limited effect on the elastic stiffness of the coupon. As the orthotropic fibres will not be further investigated in this project there will be no further elaboration on this topic.

Table A.2: Parameter study on the angular search increment where the number of fibres, the difference in number of fibres and the normalised stiffness is presented.

Angular search increment [°]	Number of fibres (Deviation)	Normalised stiffness
45	231,614 (- 23.1 %)	1.034
30	279,448 (- 7.3 %)	1.031
15	303,963 (+ 0.9 %)	1.005
10	301,296 (+- 0 %)	1

A.3 Effect of the Poisson's ratio on the elastic stiffness

One parameter that is not calibrated in the project is Poisson's ratio. As mentioned earlier it is important to check what effects the Poisson's ratio has on the solution and this parameter study is presented in this section. The analysis is done on the elastic calibration case. The Poisson's ratio for the fibre and matrix is changed both one at a time as well as changing both parameters. For comparison the elastic stiffness of the coupon has been computed and then normalised against the mechanical test coupon stiffness.

In Table A.3 the Poisson's ratio of the matrix is kept constant at the value of 0.35 and the Poisson's ratio of the fibre is varied between 0.214 and 0.45. From the table, it is observed that the normalised stiffness is deviating within 1% among all combinations of Poisson's ratio for the matrix and the fibre. Another note is that as the Poisson's ratio of the fibre increase, the coupon stiffness is decreasing.

Table A.3: Parameter study on the effect of the Poisson's ratio where the Poisson's ratio of the fibre and matrix, as well as the normalised stiffness of the coupon, is presented. The Poisson's ratio for the matrix is kept constant at 0.35.

Poisson's ratio fibre, ν_f	0.214	0.285	0.35	0.40	0.45
Poisson's ratio matrix, ν_m	0.35	0.35	0.35	0.35	0.35
Normalised stiffness	1.009	1.005	1.0	0.998	0.997

In Table A.4 the Poisson's ratio of the matrix is varying between 0.20 and 0.45 and the Poisson's ratio of the fibre is kept constant at the value of 0.35. From the table, it is observed that the maximum deviation in normalised stiffness is 2.1%. Another interesting observation is that as the Poisson's ratio for the matrix is increasing, the coupon stiffness is increasing.

Table A.4: Parameter study on the effect of the Poisson's ratio where the Poisson's ratio of the fibre and matrix, as well as the normalised stiffness of the coupon, is presented. The Poisson's ratio for the fibre is kept constant at 0.35.

Poisson's ratio fibre, ν_f	0.35	0.35	0.35	0.35	0.35
Poisson's ratio matrix, ν_m	0.20	0.275	0.35	0.40	0.45
Normalised stiffness	1.0	0.997	1.0	1.007	1.021

In Table A.5 both the Poisson's ratio of the fibre and matrix is varying. The Poisson's ratio of the fibre takes values between 0.35 and 0.45 whereas the Poisson's ratio of the matrix takes values between 0.20 and 0.30 in six different combinations. From the table, it is observed that the maximum deviation in normalised stiffness is 0.3%. In addition to this, it is observed that the normalised stiffness is more or less the same for all configurations.

Table A.5: Parameter study on mesh size where the angular search increment, the number of fibres, the difference in number of fibres and the normalised stiffness is presented.

Poisson's ratio fibre, ν_f	0.35	0.40	0.40	0.40	0.45	0.45
Poisson's ratio matrix, ν_m	0.25	0.20	0.25	0.30	0.20	0.25
Normalised stiffness	0.997	0.999	0.997	0.997	0.999	0.997

To summarise this parameter study it should be pointed out that the effect of changing the Poisson's ratio is limited on the results. This analysis has been made on the elastic isotropic case and the outcome is that the solution is more or less independent of the value of the Poisson's ratio regarding the elastic coupon stiffness. From this, the Poisson's ratio is set at the value of 0.35 for both fibre and matrix in the continuation of the project.

B

XAE results

In this appendix, the results from the XAE process of Sample 2 and Sample 3 are presented in a similar way as the results for Sample 1 in Section 4.1. The main results are a reconstructed image from the image acquisition, a histogram of the grey-scale image data, a figure showing the phase segmentation, an image of the mesh, a table of volume fractions and an image where fibre orientations are visible.

B.1 Sample 2: KE1450 2 mm

A reconstructed image of Sample 2 is presented in Figure B.1 below. The scan time of the bundle was approximately 12 hours and the image data (.txm file) file size was 16.4 GB.

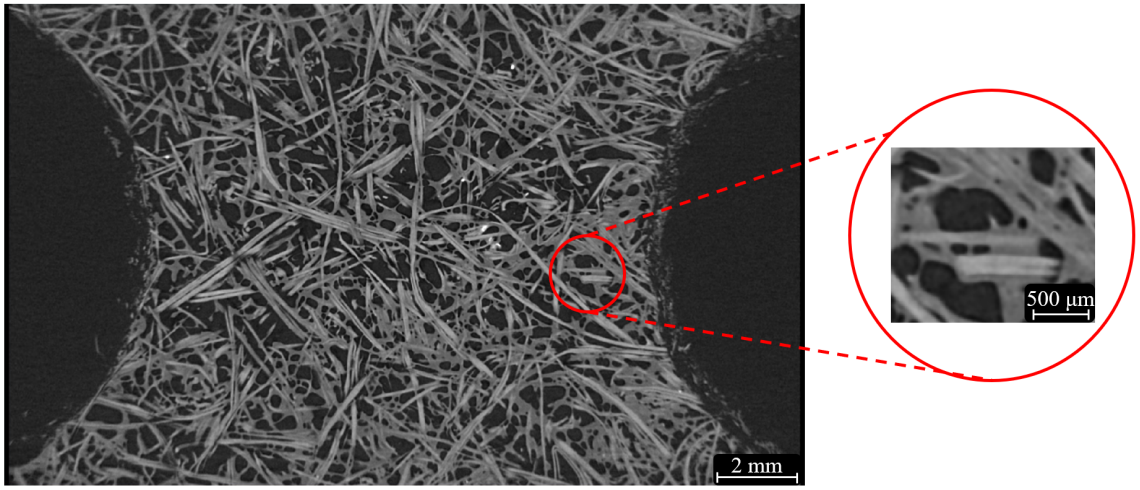

Figure B.1: Reconstructed image of Sample 2. Images are from the commercial software RETOMO.

The grey-scale threshold for void - matrix is 2850 and the threshold for matrix - fibre is 3575. The grey-scale values are collected in a histogram, presented in Figure B.2 below.

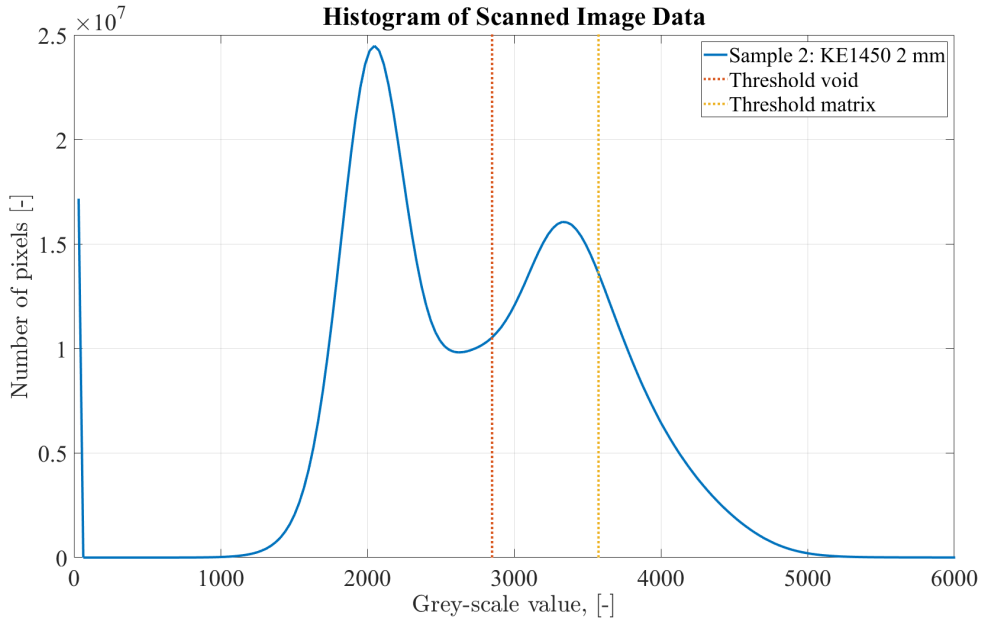

Figure B.2: Histogram of the grey-scale image data from the image acquisition for Sample 2.

The phase segmentation is presented in Figure B.3 where the three phases void, matrix and fibre are indicated by three different colours. The blue parts are surrounding air and voids inside the composite, the red parts are matrix and the yellow are fibres. This phase segmentation is gained from the threshold values presented in the previous paragraph.

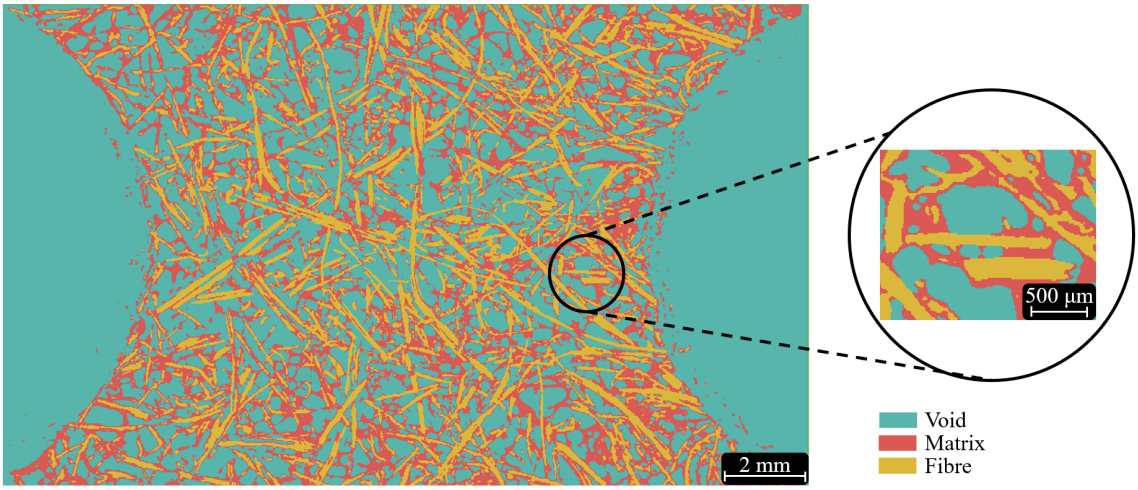

Figure B.3: Segmentation of the three phases void, matrix and fibre for Sample 2.

The generated mesh is presented in Figure B.4 where each phase is presented with a unique colour. The voids inside the composite are the black parts, the matrix material is the grey parts and the fibres are white. With a sub-sampling rate of 5, the model has 3,187,728 8-noded hexahedron elements.

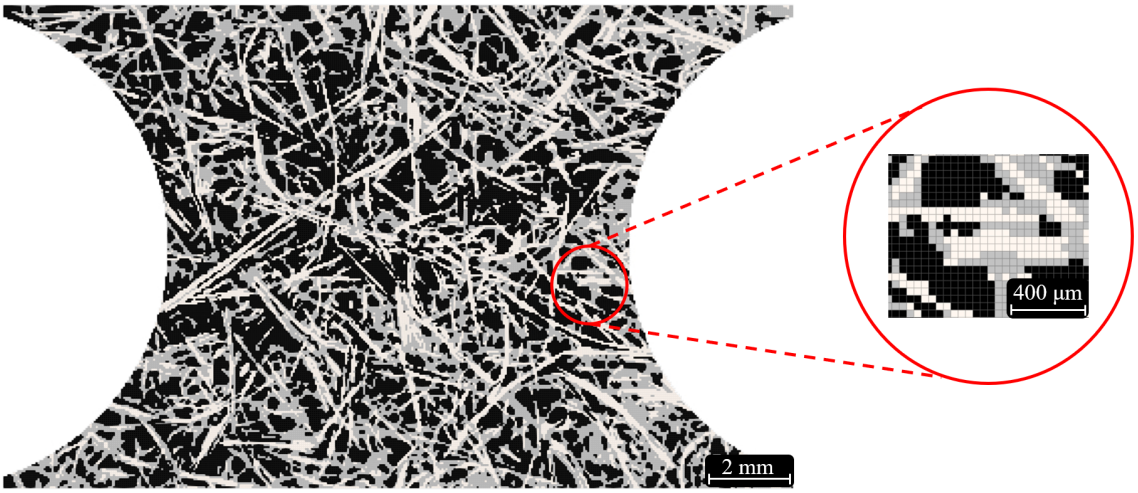

Figure B.4: The generated mesh for Sample 2. The total number of elements is 3,187,728.

The volume fractions of void, matrix and fibre are presented in Table B.1. It is observed that the void volume fraction is 1.6% lower in the simulation compared to the analytical value. Further, it is noted that the matrix fraction is 0.5% lower and the fibre fraction 3.4% higher compared to the analytical volume fractions.

Table B.1: Comparison of simulated and analytical volume fractions of void, matrix and fibre for Sample 2.

	Void [%]	Matrix [%]	Fibre [%]
Analytical	38.3	38.3	23.4
FE Simulation	37.7	38.1	24.2

To study the results from the fibre tracking described in Section 3.2.3 an image, where the element orientations are visible, is presented in Figure B.5. The image is the same cut-out as presented in the rightmost part of Figure B.4 where a fraction of a fibre is cut out in order for the orientations to be visible. The red arrows indicate the direction of the fibre along the global x-axis.

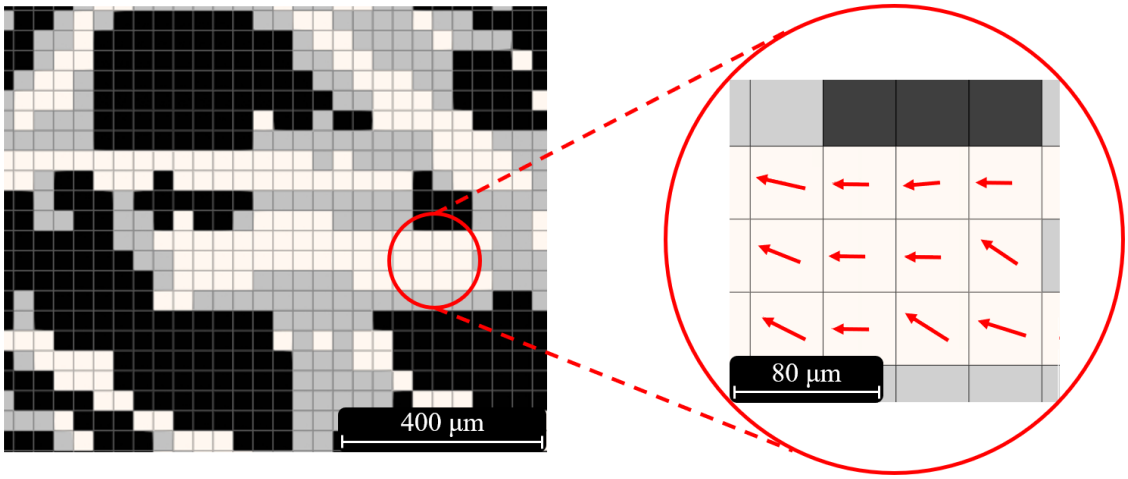

Figure B.5: Fibre orientations are visible for each element in Sample 2. The red arrows indicate the direction along the global x-axis.

B.2 Sample 3: KE1450 1.7 mm

A reconstructed image of Sample 3 is presented in Figure B.6 below. The scan time of the bundle was approximately 12 hours and the image data (.txm file) file size was 16.3 GB.

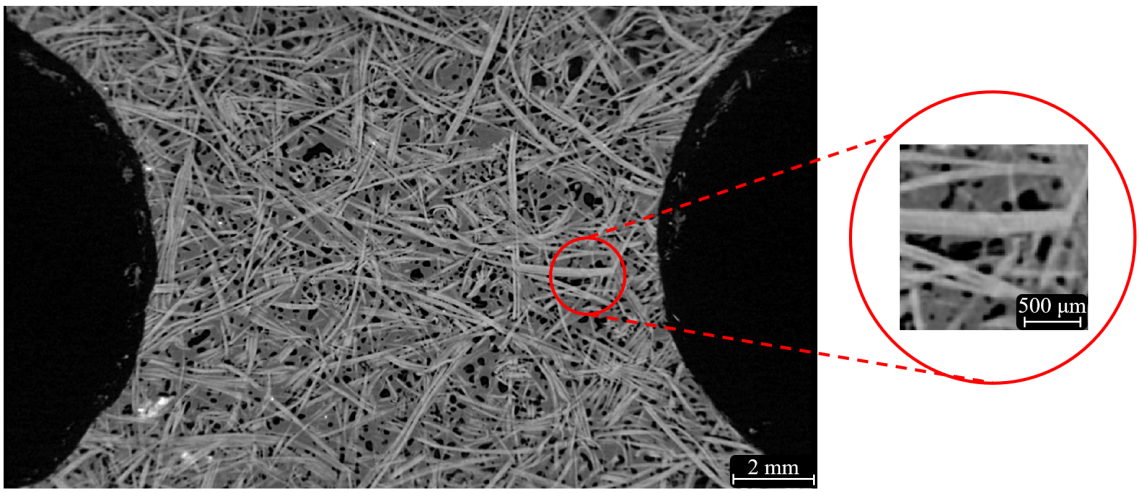

Figure B.6: Reconstructed image of Sample 3. Images are from the commercial software RETOMO.

The grey-scale threshold for void - matrix is 10350 and the threshold for matrix - fibre is 12250. The grey-scale values are collected in a histogram, presented in Figure B.7 below.

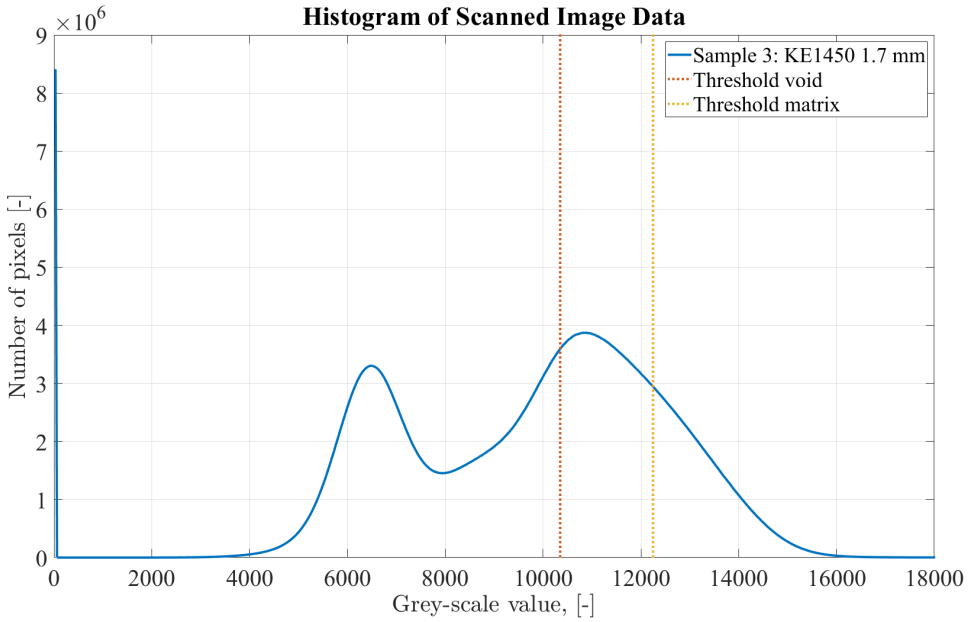

Figure B.7: Histogram of the grey-scale image data from the image acquisition for Sample 3.

The phase segmentation is presented in Figure B.8 where the three phases void, matrix and fibre are indicated by three different colours. The blue parts are surrounding air and voids inside the composite, the red parts are matrix and the yellow are fibres. This phase segmentation is gained from the threshold values presented in the previous paragraph.

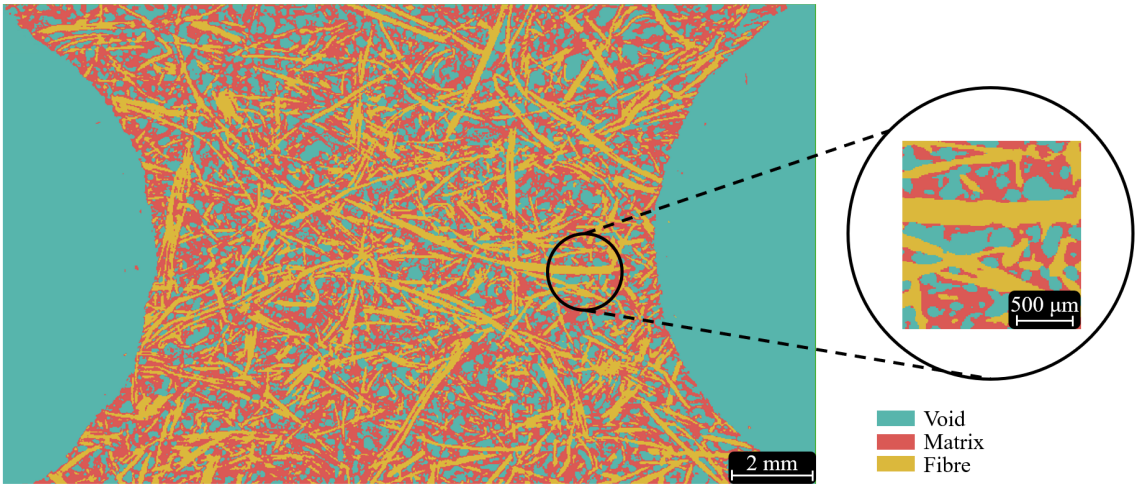

Figure B.8: Segmentation of the three phases void, matrix and fibre for Sample 3.

The generated mesh is presented in Figure B.9 where each phase is presented with a unique colour. The voids inside the composite are the black parts, the matrix material is the grey parts and the fibres are white. With a subsampling rate of 5, the model has 1,926,912 8-noded hexahedron elements.

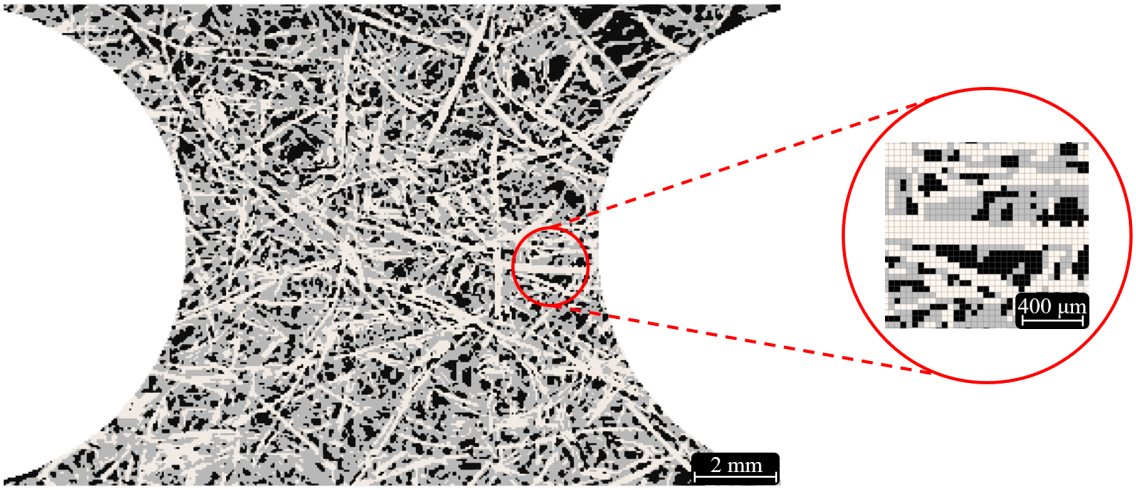

Figure B.9: The generated mesh for Sample 3. The total number of elements is 1,926,912

The volume fractions of void, matrix and fibre are presented in Table B.2. It is observed that the void volume fraction is 4.2% lower in the simulation compared to the analytical value. Further, it is noted that the matrix fraction is 3.8% higher and the fibre fraction 2.2% lower compared to the analytical volume fractions.

Table B.2: Comparison of simulated and analytical volume fractions of void, matrix and fibre for Sample 3.

	Void [%]	Matrix [%]	Fibre [%]
Analytical	27.4	45.1	27.5
FE Simulation	26.3	46.8	26.9

To study the results from the fibre tracking described in Section 3.2.3 an image, where the element orientations are visible, is presented in Figure B.10. The image is the same cut-out as presented in the rightmost part of Figure B.9 where a fraction of a fibre is cut out in order for the orientations to be visible. The red arrows indicate the direction of the fibre along the global x-axis.

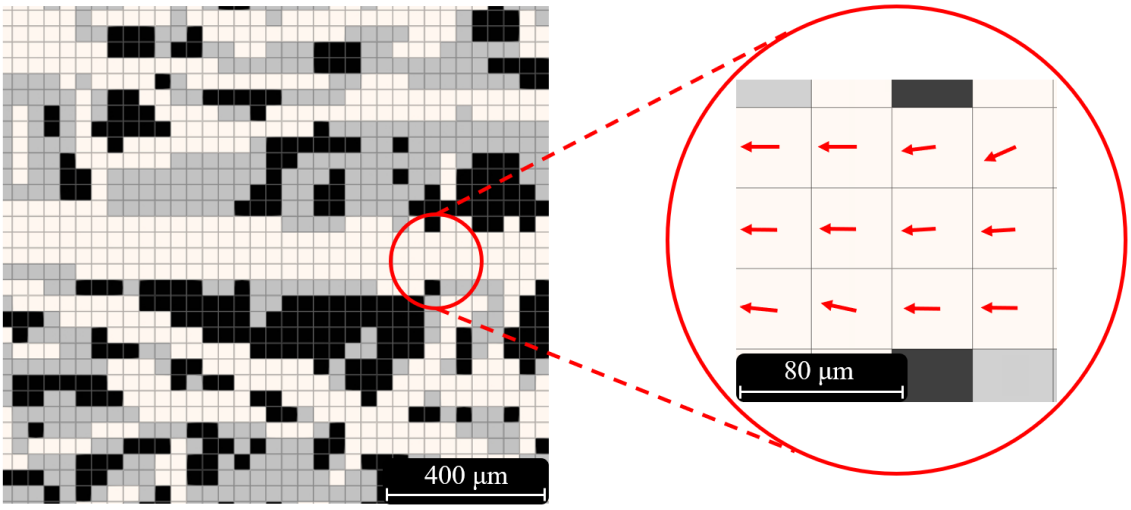

Figure B.10: Fibre orientations are visible for each element in Sample 3. The red arrows indicate the direction along the global x-axis.

DEPARTMENT OF INDUSTRIAL AND MATERIALS SCIENCE
CHALMERS UNIVERSITY OF TECHNOLOGY
Gothenburg, Sweden
www.chalmers.se

CHALMERS
UNIVERSITY OF TECHNOLOGY